Evaluating Metallic Material Performance in High-pressure Hydrogen Gas

API TECHNICAL REPORT 21C
FIRST EDITION, JULY 2025

Special Notes

API publications necessarily address problems of a general nature. With respect to particular circumstances, local, state, and federal laws and regulations should be reviewed. The use of API publications is voluntary. In some cases, third parties or authorities having jurisdiction may choose to incorporate API standards by reference and may mandate compliance.

Neither API nor any of API's employees, subcontractors, consultants, committees, or other assignees make any warranty or representation, either express or implied, with respect to the accuracy, completeness, or usefulness of the information contained herein, or assume any liability or responsibility for any use, or the results of such use, of any information or process disclosed in this publication. Neither API nor any of API's employees, subcontractors, consultants, or other assignees represent that use of this publication would not infringe upon privately owned rights.

Users of this standard should not rely exclusively on the information contained in this document. Sound business, scientific, engineering, and safety judgment should be used in employing the information contained herein.

API is not undertaking to meet the duties of employers, manufacturers, or suppliers to warn and properly train and equip their employees, and others exposed, concerning health and safety risks and precautions, nor undertaking their obligations to comply with authorities having jurisdiction.

API publications may be used by anyone desiring to do so. Every effort has been made by the Institute to ensure the accuracy and reliability of the data contained in them; however, the Institute makes no representation, warranty, or guarantee in connection with this publication and hereby expressly disclaims any liability or responsibility for loss or damage resulting from its use or for the violation of any authorities having jurisdiction with which this publication may conflict.

API publications are published to facilitate the broad availability of proven, sound engineering and operating practices. These publications are not intended to obviate the need for applying sound engineering judgment regarding when and where these publications should be utilized. The formulation and publication of API publications is not intended in any way to inhibit anyone from using any other practices.

Any manufacturer marking equipment or materials in conformance with the marking requirements of an API standard is solely responsible for complying with all the applicable requirements of that standard. API does not represent, warrant, or guarantee that such products do in fact conform to the applicable API standard.

Foreword

Nothing contained in any API publication is to be construed as granting any right, by implication or otherwise, for the manufacture, sale, or use of any method, apparatus, or product covered by letters patent. Neither should anything contained in the publication be construed as insuring anyone against liability for infringement of letters patent.

Suggested revisions are invited and should be submitted to the Standards Department, API, 200 Massachusetts Avenue NW, Suite 1100, Washington, DC 20001, standards@api.org.

Contents

Figures

Tables

Evaluating Metallic Material Performance in High-pressure Hydrogen Gas

1 Scope

1.1 General

Understanding the fracture behavior of metallic materials in high-pressure H_2 environments can be useful for selection of materials in underground H_2 storage. Currently, there are sparse data on fracture mechanics of metallic materials typically used in oil and gas well construction when subject to high-pressure H_2 gas environments. This test program is an effort to generate data to provide some insight into testing procedures and material behavior, which over time could help the industry in evaluation and selection of materials in such service.

2 Normative References

There are no normative references in the document.

3 Acronyms, Abbreviations, and Symbols

σ	stress
K_{th}	threshold stress intensity factor
CMOD	crack mouth opening displacement
COD	crack opening displacement
C(T)	compact tension
DCPD	direct current potential drop
EDM	electrical discharge machining
El	elongation
FCGR	fatigue crack growth rate
FT	fracture toughness
H_2	hydrogen
H_2O	water
H_2S	hydrogen sulfide

HE	hydrogen embrittlement
He	helium
HRC	hardness in Rockwell C scale
ID	identification number
N_2	nitrogen
NaCl	sodium chloride
NaOH	sodium hydroxide
O_2	oxygen
OD	outside diameter
Pd	palladium
PH	precipitation hardened
PTFE	polytetrafluoroethylene
Q&T	quench and temper
RA	reduction in area
RT	room temperature
SCE	saturated calomel electrode
SCFH	standard cubic feet per hour
SCGR	static crack growth rate
SEM	scanning electron microscope
SSR	slow strain rate
SWCP	seawater under cathodic potential
TTF	time to failure
UTS	ultimate tensile strength
YS	yield strength

4 Background

4.1 General

Achieving net-zero carbon emissions will require a transformation of the power and energy infrastructure, including the transition to hydrogen (H_2) as a fuel of the future. While it is anticipated that H_2 in near term will be used in primarily smaller-scale applications—such as portable power, public transportation vehicles, and space applications—it is foreseeable that the future use of H_2 would include use in industries such as steel, cement, shipping and other transportation, etc. This setup will require an infrastructure that can deliver H_2 from its source to the end users in large volumes. Therefore, providing H_2 storage, transmission, and delivery infrastructure will be critical for such applications. Currently, there are ongoing efforts in the industry to understand and overcome challenges than can be presented for use of H_2.

In addition to using pipeline network for H_2 transmission, large-scale storage options beyond surface storage tanks or cryogenic vessels are needed. Underground storage wells have been successfully used for storing large volumes of natural gas (methane) for many decades now to facilitate use of it in power generation and feedstock for chemical plants on demand. A similar approach with H_2 could provide a low- or no-carbon fuel for these applications. Geological formations, such as salt caverns, depleted wells, mines, aquifers, hard rock caverns, and mine seams, can provide a means to store large volumes of H_2 and thus would have significant impact in providing the required energy in an H_2-based economy. The benefits and drawbacks of each of the previously listed geological formations for H_2 storage have been extensively reviewed [1-5]. Despite some similarities between the storage of natural gas and H_2 gas, underground well storage of H_2 can be more complex due to physical and chemical properties differences between the two cases. Some of the differences, such as the smaller size of H_2 molecule and lower viscosity, can lead to leaks; chemical reactions during storage could lead to production of other corrosive elements, such as hydrogen sulfide (H_2S), acids, etc. All these could factor into material choices for such applications.

For use of metallic materials in underground storage wells, concerns of hydrogen embrittlement (HE) from exposure to high-pressure H_2 gas need to be addressed. Embrittlement can cause sudden, catastrophic failure of equipment. Hence, understanding the HE susceptibility of various metals that could be used for underground H_2 storage would be very important for optimum material selection. In this testing program, the main objective was to evaluate test methods that can be used for understanding HE resistance in high-pressure H_2 gas and also provide comparison of performance of metallic materials typically used for underground storage well construction.

4.2 Test Program

4.2.1 Materials

The work group decided to test one grade of low-alloy steel and one grade of precipitation-hardenable nickel-based alloy to study the effect of high-pressure H_2 gas on two distinct material systems. One heat of low-alloy steel grade AISI (American Iron and Steel Institute) 4140 heat-treated via quench-and-temper (Q&T) treatment to 110 ksi specified minimum yield strength, and one heat of Alloy 718-120 solution annealed and aged per API 6ACRA were selected [6]. The details of material selected are given in Table 1, along with chemical composition in Table 2 and mechanical properties in Table 3 at mid-radius. Both the selected heats, while very different material grades, were of similar size, product form, and actual yield strengths. The 4140-110 heat had actual yield strength close to 140 ksi, which is typically the maximum yield strength associated with similar grades, such as API 5CT [7].

Table 1—Description of Materials Used for Testing

Grade	Product and Size	Condition
4140-110	5-in. outer diameter (OD) bar	Q&T to 110 ksi minimum yield strength (MY)
Alloy 718-120	5-in. OD bar	Solution annealed and aged per API 6ACRA

Table 2—Chemical Composition (wt%)

Grade	C	Mn	Si	Cr	Mo	Ni	P	S
4140-110	0.42	0.95	0.26	1.06	0.23	0.18	0.011	0.004
Alloy 718-120	0.013	0.06	0.05	18.2	2.90	53.5	0.008	0.000001

Table 3—Mechanical Properties of the Material Grades

Grade	Yield Strength (YS), 0.2% offset	UTS, (ksi)	% El	% RA	Hardness in Rockwell "C" Scale (HRC)
4140-110	137.0	154.4	18.0	57.0	35
Alloy 718-120	135.2	181.8	27.6	40.2	38

4.2.2 Test Environment

Testing was done at 100-bar (1450-psi) H_2 gas pressure at room temperature (RT). The pressure was based on somewhat typical underground H_2 storage well pressure, especially in salt cavern storage and readily available multiple-lab facilities for the anticipated test program duration. Testing at RT was done mainly with the reasoning that HE phenomena tend to be more active closer to RT for many metallic material grades, and RT was a good reference to compare different material systems. Testing was done with 99.999% pure dry H_2 gas with oxygen (O_2) <1 ppm, water vapor (H_2O) <10 ppm, and no other intentional impurities. This was selected to baseline a test environment gas for comparison testing. While the effect of impurities is a relevant topic the consensus was to first develop confidence in test methods with more standard test environments and this could be a future consideration.

4.2.3 Test Methods

The below sections provide a summary of the test methods. more details are available in Annex A and Annex B.

4.2.3.1 Slow Strain Rate (SSR)

Testing for SSR via ASTM G142 at target strain rate of 10^{-5} s^{-1}. Based on the scope of testing program; testing for 4140-110 grade was done at Lab A, while testing of Alloy 718-120 was done at Lab B [8]. Testing was to be done with at three inert specimens and three environmental specimens for each material grade selected; with specimens extracted from mid-radius location.

4.2.3.2 Fracture Toughness (FT)

Testing for FT was done via ASTM E1820 via slow rising displacement method using compact tension [C(T)] specimens [10]. Testing was also to be done at two different labs (A and B) to provide understanding into possible variation in the results between two independent laboratories.

The specimens were extracted at mid-radius location for both grades in the transverse direction and the notch direction was C-L, per ASTM E1823 [11]. Testing was to be done with at least one inert specimen and two environmental specimens for each material grade selected. The initial target K rate of 1 $MPa.m^{1/2}.h^{-1}$ (0.01 $N.mm^{-3/2}.s^{-1}$) for selected for environmental testing while the inert testing K rate value could be higher.

Lab A used C(T) specimens for both inert and environmental tests with W=1 in. and B=0.5 in. The initial a/W=0.5 in. (where a is the total crack length including the pre-crack; the nominal notch depth was 0.45 in. with 0.05-in. pre-cracking in air) and specimens were side-grooved by 5% of the thickness on each side. The samples were side-grooved prior to pre-cracking.

Lab B used C(T) specimens for inert tests with W=2 in. and B=1 in., while specimens for environmental tests had W=1.25 in. and B=0.3 in. For both cases, the initial a/W=0.5 in. (where a is the total crack length including the pre-crack; the nominal notch depth was 0.45 in. with 0.05 in. pre-cracking in air) and specimens were side-grooved by 10% of the thickness on each side. The samples were side-grooved prior to pre-cracking.

4.2.3.3 H_2 Permeation

H_2 permeation testing was performed in a specialized stainless-steel high-pressure autoclave test apparatus. Testing was performed using an electrochemical technique per ASTM G148 [12]. Like SSR testing, permeation testing of 4140-110 grade was done at Lab A while testing of Alloy 718-120 was done at Lab B.

5 Summary of Testing Program Results

5.1 General

The testing scope consisted of performing SSR tests, H_2 permeation tests, and rising displacement FT tests. All environmental tests were performed at RT in 100-bara H_2.

5.2 SSR Results

The SSR results for 4140-110 grade performed at strain rate of 1.25×10^{-5} s^{-1} are shown in Figure 1(a) and summarized in Tables 4(a) and 4(b). While the initial target strain rate was10^{-5} s^{-1}, the actual testing strain rate ended up being a bit higher. Several variables, such as ultimate tensile strength (UTS), time to failure (TTF), total % elongation, % plastic elongation, % reduction in area (RA), and the ratio of these variables in H_2 to in nitrogen (N_2, inert), were measured from the test. As shown, except for the UTS, all other variables showed reduction of values for the samples tested in H_2 with % RA showing the highest drop when compared to inert test results, indicating there is an effect from the high-pressure H_2. The specimens tested in H_2 exhibited secondary cracking on the gauge length of the specimen, as shown in Figure 1(b).

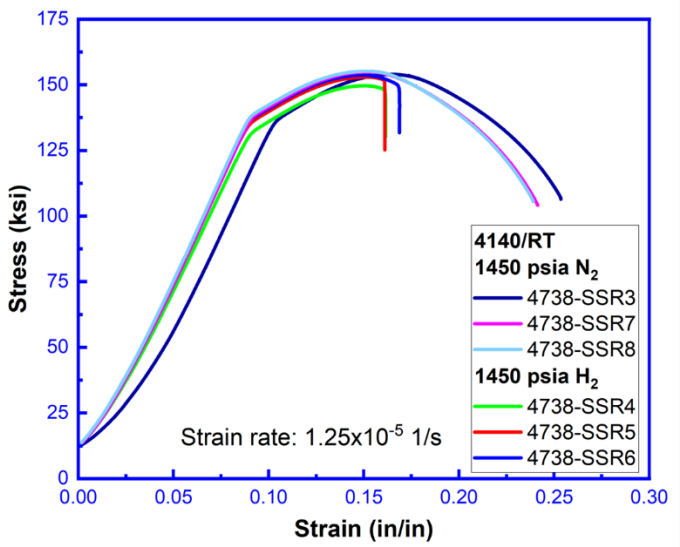

Figure 1(a)—Stress-strain Curves for 4140-110 SSR

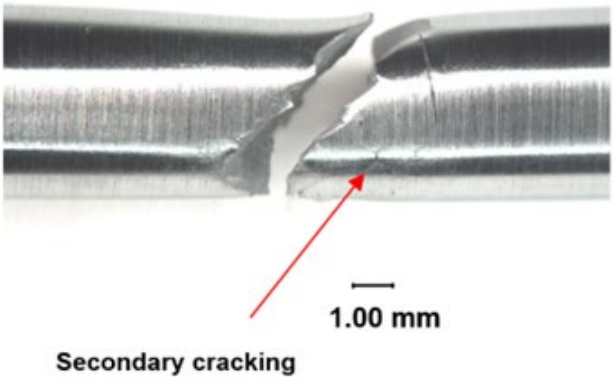

Figure 1(b)—Secondary Cracking Seen in Gauge Section of 4140-110 H_2 SSR Specimen

Table 4(a)—SSR Testing Results for 4140-110

Env.	UTS (ksi)	TTF (h)	Total Elong. (%)	Plastic Elong. (%)	Red. of Area (RA) (%)	Avg. UTS (ksi)	Avg. TTF (h)	Avg. Total Elong. (%)	Avg. Plastic Elong. (%)	Avg. RA (%)
N_2	154.0	5.6	25.0	18.4	55.0	154.7	5.4	24.3	17.7	56.2
N_2	154.9	5.4	24.1	17.4	56.1					
N_2	155.2	5.3	23.9	17.2	57.6					
H_2	149.7	3.6	16.2	7.5	14.0	152.2	3.7	16.4	7.9	12.0
H_2	153.0	3.6	16.1	7.8	8.2					
H_2	153.8	3.8	16.8	8.4	13.9					

Table 4(b)—SSR Ratios for 4140-110

Env.	UTS ratio	TTF ratio	Total Elong. ratio	Plastic Elong. ratio	RA ratio	Avg. UTS ratio	Avg. TTF ratio	Avg. Total Elong. ratio	Avg. Plastic Elong. ratio	Avg. RA ratio
H_2	0.97	0.67	0.67	0.42	0.25	0.98	0.69	0.67	0.45	0.21
H_2	0.99	0.67	0.66	0.44	0.15					
H_2	0.99	0.70	0.69	0.47	0.25					

The scanning electron microscope (SEM) photomicrographs of the 4140-110 steel tested in inert (N_2) and H_2 are shown in Figures 2 and 3, respectively. The SSR specimen fracture surface in inert medium showed ductile behavior with presence of microvoid coalescence showing the material has good ductility in inert environment. The SSR specimen fracture surface in the H_2 test showed a brittle transgranular fracture morphology with secondary cracking. This shows that testing via SSR in the presence of H_2, the fracture morphology of 4140-110 changes from ductile to brittle behavior.

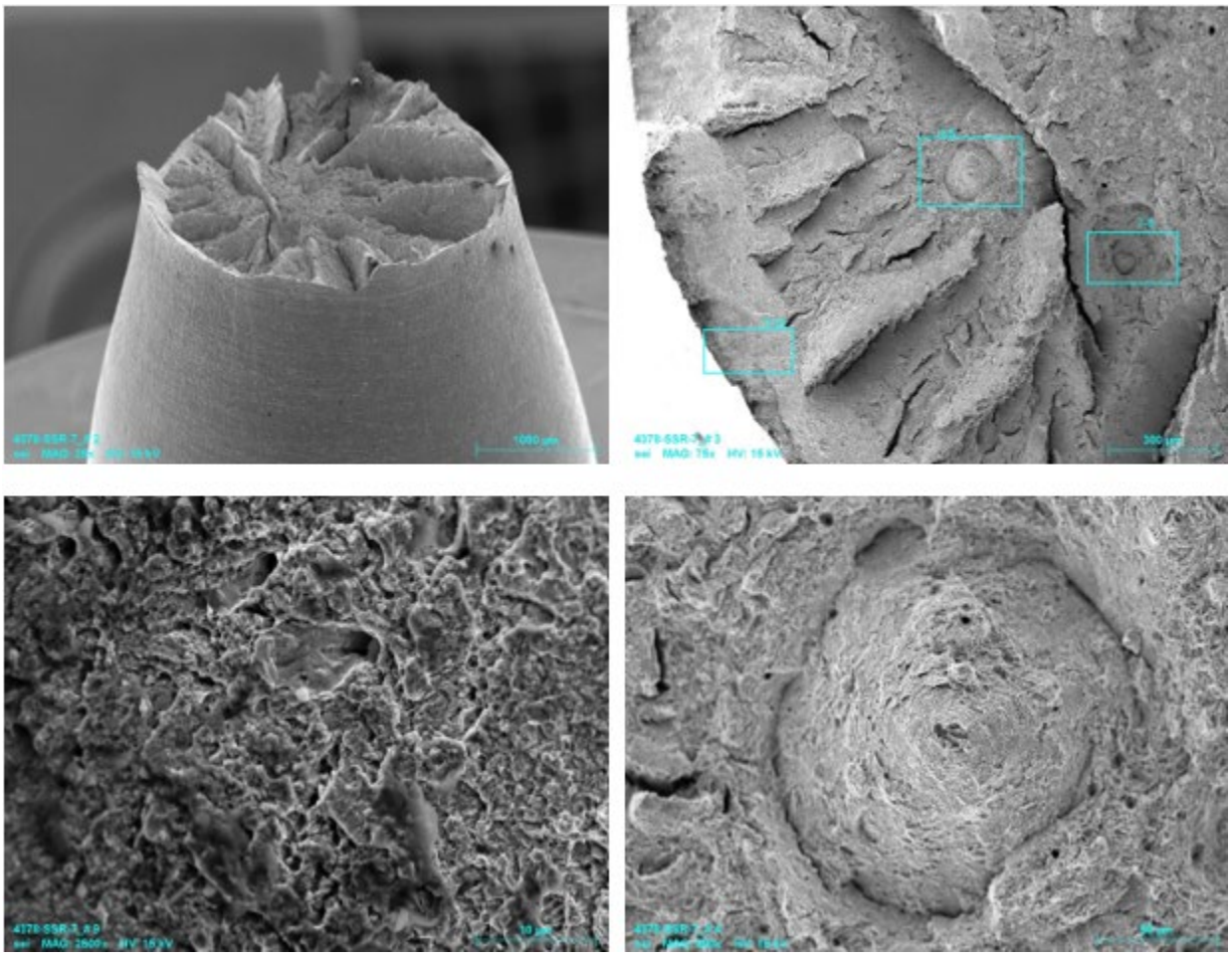

Figure 2—SEM Photomicrographs of the SSR Sample for 4140-110 Steel Tested in Inert

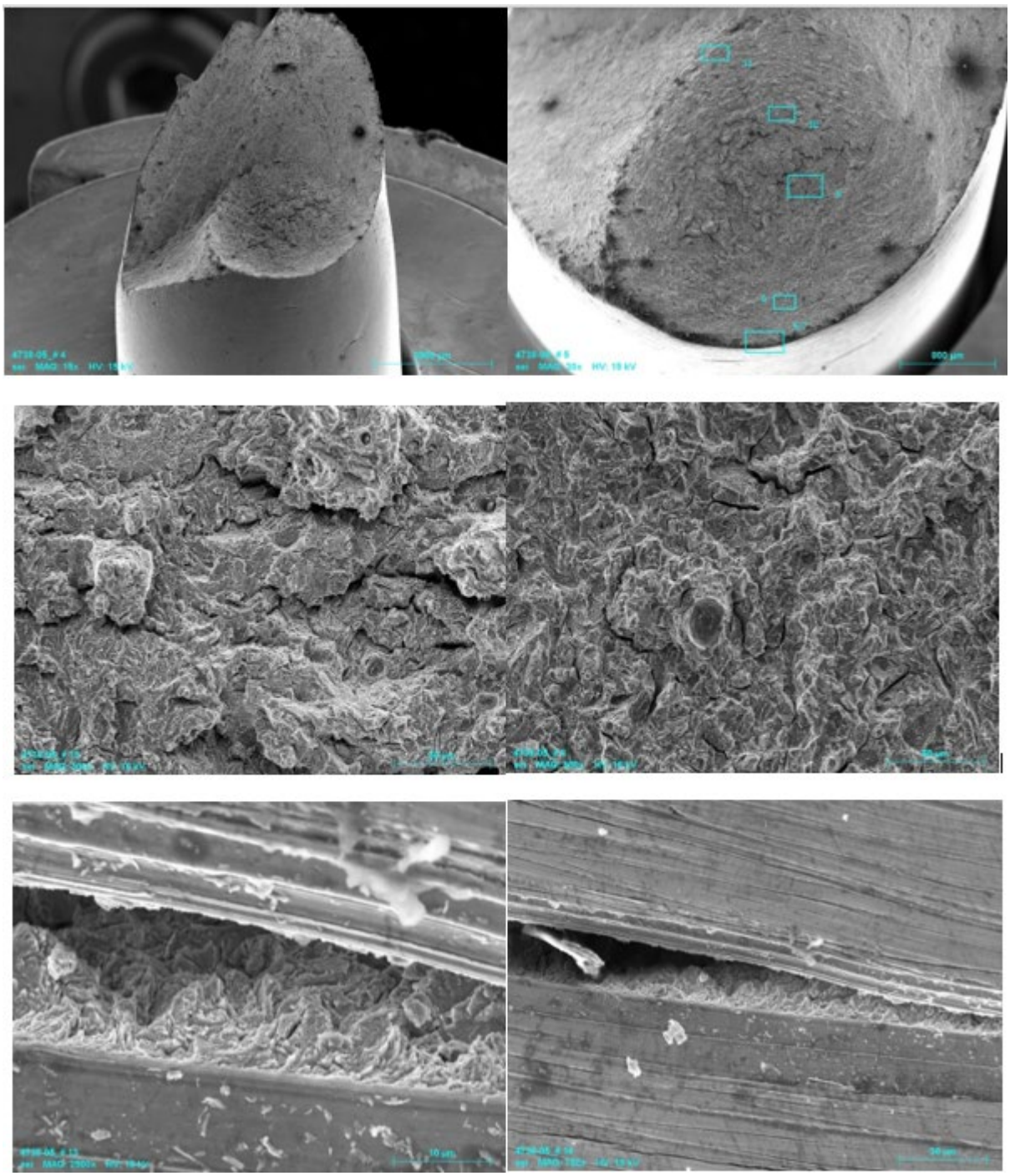

Figure 3—SEM Photomicrographs of the SSR Sample for 4140-110 Steel Tested in 100-bara H_2

The SSR results for Alloy 718-120 performed at strain rate of 2x10-5 s^{-1}. are shown in Figure 4 and summarized in Tables 5(a) and 5(b). While the initial target strain rate was 1x10-5 s^{-1}, the actual testing strain rate ended up being a bit higher. Several variables, such as UTS, TTF, total % elongation, % plastic elongation, % RA, and the ratio of these variables in H_2 to in helium (He, inert) were measured from the test. The H_2 gas had limited effect on the ultimate tensile stress for the H_2 gas tests relative to the He (inert) tests. The material ductility in terms of elongation, reduction of area was lower in high-pressure H_2 compared to inert with the decrease in elongation more than in RA.

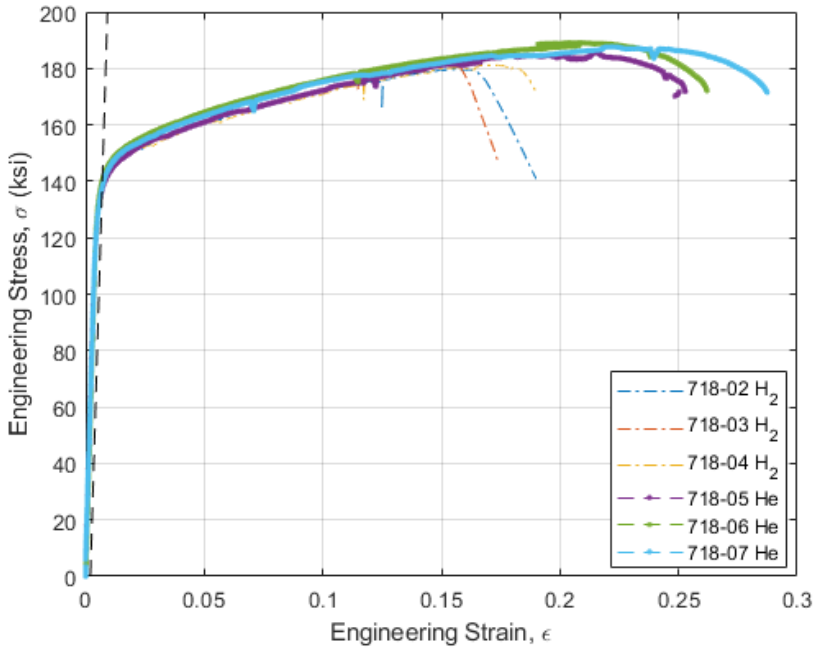

Figure 4—Stress-strain Curves of Alloy 718-120 SSR

Table 5(a)—SSR Testing Results for Alloy 718-120

Env.	UTS (ksi)	TTF (h)	Total Elong. (%)	Plastic Elong. (%)	Red. of Area (RA) (%)	Avg. UTS (ksi)	Avg. TTF (h)	Avg. Total Elong. (%)	Avg. Plastic Elong. (%)	Avg. RA (%)
He	188.0	3.6	39.0	24.9	26.9	189.0	3.9	38.7	26.3	26.2
He	190.0	3.9	38.3	25.7	27.2					
He	189.0	4.2	38.7	28.3	24.6					
H_2	180.0	2.3	21.8	15.4	17.4	181.7	2.3	5.5	15.6	20.2
H_2	183.0	2.2	21.8	15.3	21.1					
H_2	182.0	2.4	23.5	16.2	22.0					

Table 5(b)—SR Ratios for Alloy 718-120

Env.	UTS ratio	TTF ratio	Total Elong. ratio	Plastic Elong. ratio	RA ratio	Avg. UTS ratio	Avg. TTF ratio	Avg. Total Elong. ratio	Avg. Plastic Elong. ratio	Avg. RA ratio
H_2	0.95	0.58	0.56	0.58	0.66	0.96	0.59	0.58	0.59	0.77
H_2	0.97	0.56	0.56	0.58	0.81					
H_2	0.96	0.62	0.61	0.62	0.84					

The SEM photomicrographs of Alloy 718-120 tested in inert (He) and in H_2 are shown in Figures 5 and 6, respectively. The SSR specimen fracture surface in the inert medium showed presence of microvoid

coalescence throughout the entire cross section of the fracture surface, thus exhibiting a ductile behavior. In case of the SSR specimen fracture surface in the H_2 test; the outer circumferential regions showed presence of intergranular fracture morphology with secondary cracking, indicating more brittle behavior, while the central portion of the specimen showed more ductile behavior with the presence of microvoid coalescence. This difference at the two sections may be due to the slower diffusion rate of H_2 in an austenitic microstructure, such as that found in in Alloy 718-120[13].

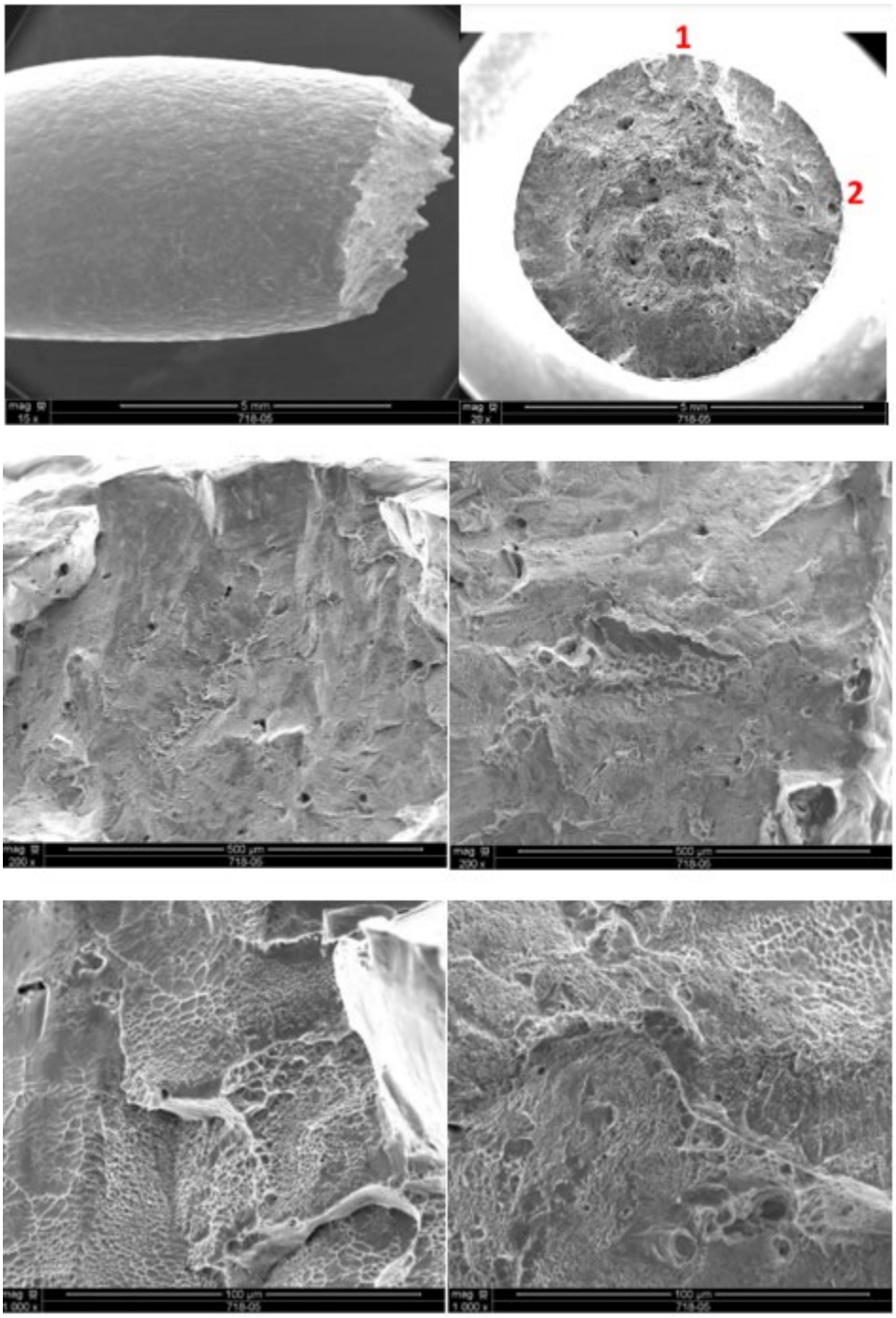

Figure 5—SEM Photomicrographs of the SSR Sample for Alloy 718-120 Tested in Inert

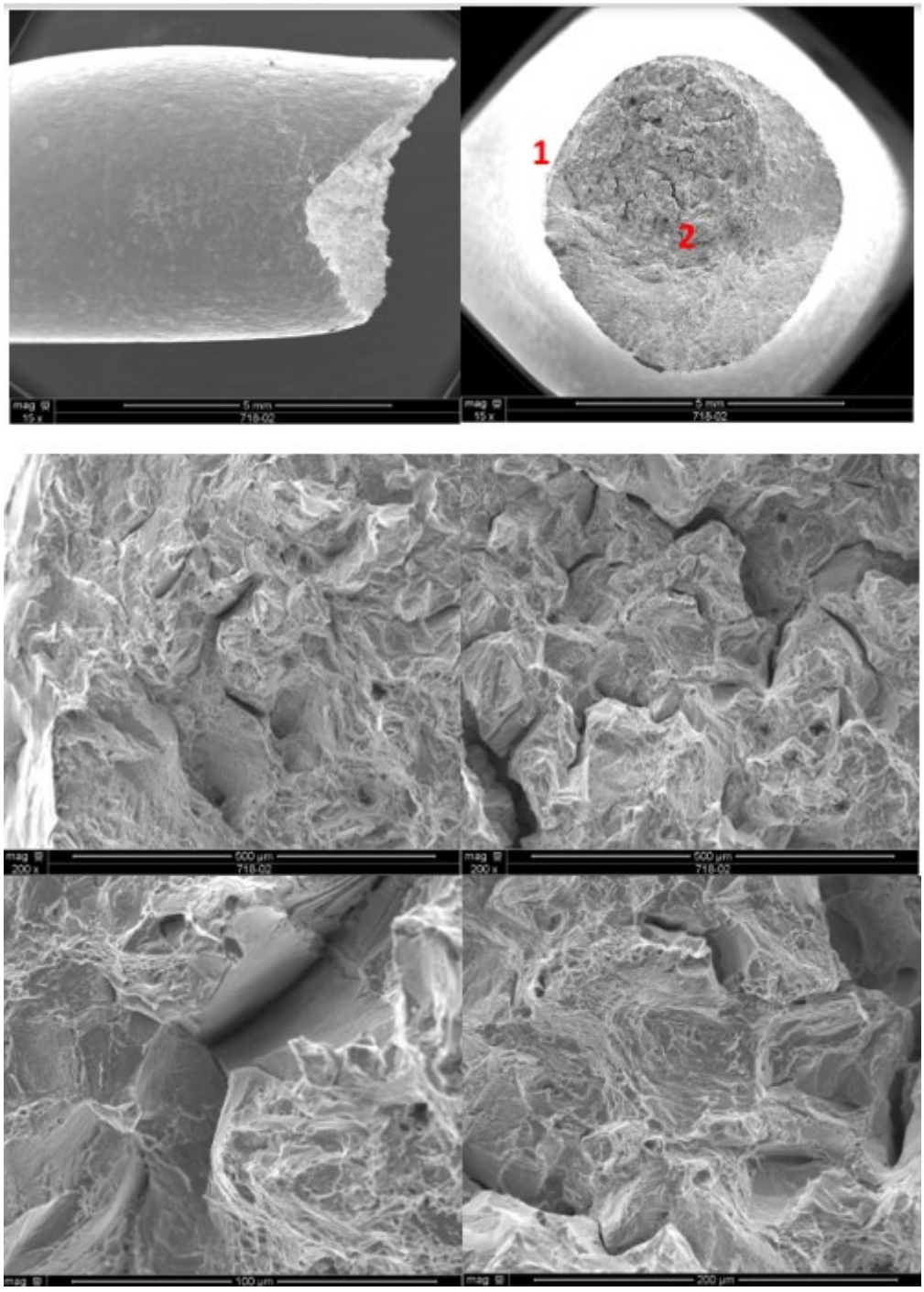

Figure 6—SEM Photomicrographs of the SSR Sample for Alloy 718-120 Tested in 100-bara H_2

5.3 FT Results

4140-110 and Alloy 718-120 were tested for FT evaluation in an inert (N_2/air) environment and in 100-bar gaseous H_2 environment at two different labs (A and B). While the K rate for H_2 was initially targeted as 0.01 $N.mm^{-3/2}.s^{-1}$, the tested K rates for the tests in H_2 differed between the two labs. No specific K rate for inert was specified, as the K-values in inert are typically not rate-dependent. At Lab A, all tests in the

inert environment (N_2) were performed under an initial K rate of approximately 3.8 $N.mm^{-3/2}.s^{-1}$, whereas the environmental tests were performed at an initial K rate of 0.01 $N.mm^{-3/2}.s^{-1}$. The inert environmental tests performed at Lab B were done under an initial K rate of ~12 $N.mm^{-3/2}.s^{-1}$. At Lab B, the H_2 tests on Alloy 718-120 were performed at an initial K rate of 0.02 $N.mm^{-3/2}.s^{-1}$ and the tests on 4140-110 steel were done at an initial K rate of 0.003 $N.mm^{-3/2}.s^{-1}$.

5.3.1 4140-110 Results

4140-110 steel was ductile when tested in the inert environment, but showed a more brittle behavior when tested in H_2, with the samples breaking in two halves with unstable crack extension at relatively low load values. Thus, J-R curves were not obtained for 4140-110 steel samples in H_2. Rather, elastic K_{IC} values were calculated following the instructions in ASTM E399 and ASTM E1820 for the samples tested in H_2. Figure 7 shows the load vs. crack mouth opening displacement (CMOD) curve of 4140-110 tested in inert and H_2 at Lab A, while Figure 8 shows the same when tested in H_2 at Lab B.

The FT results for 4140-110 from two labs are summarized in Table 6 and also compared in Figure 9 as a function of the K rates.. The toughness values in H_2 show clear dependency on the K rates at which the tests were performed with lower K rates leading to lower toughness. The data clearly show the significant reduction of the toughness for the 4140-110 in 100-bara H_2 compared to the inert environment.

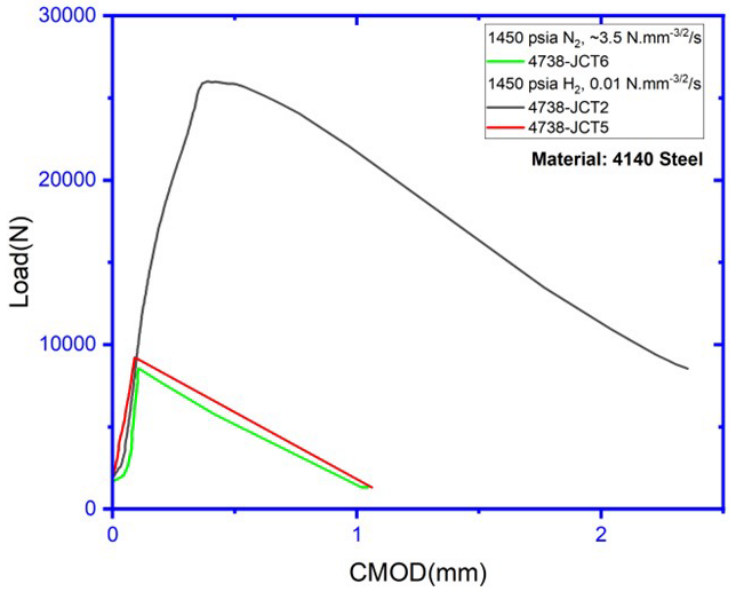

Figure 7—Load vs. CMOD for 4140-110 in Inert and H_2 from Lab A

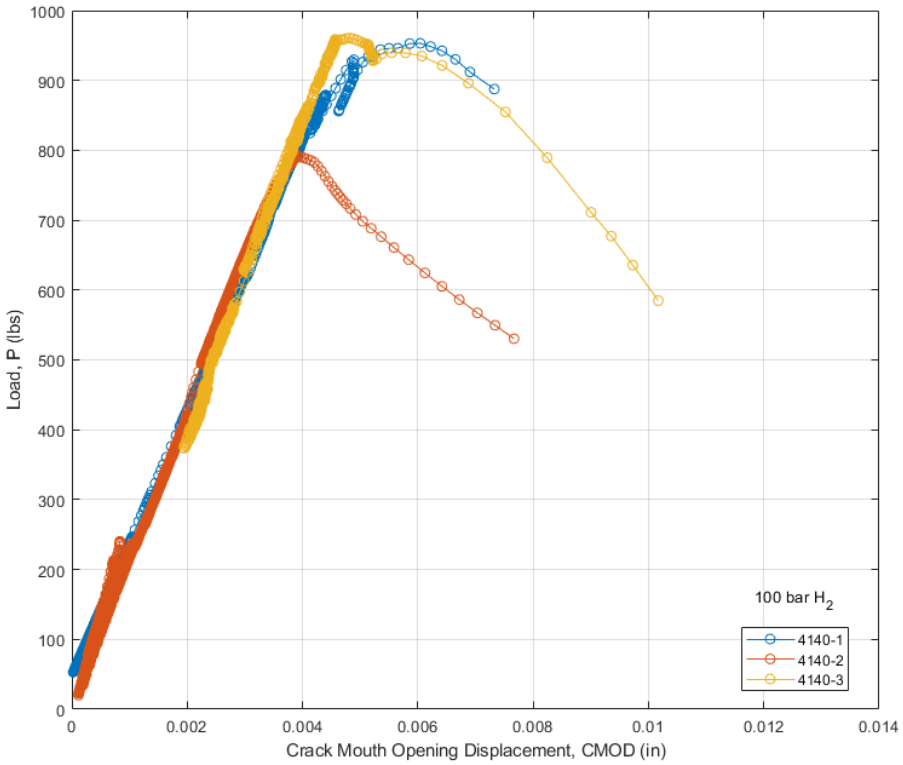

Figure 8—Load vs. CMOD for 4140-110 in H_2 from Lab B

Table 6—Summary of FT Results for 4140-110

Grade	dK/dt (N.mm$^{-3/2}$.s^{-1})	K_{IC} (ksi.in$^{1/2}$)	Test Lab	Env.
4140-110	3.8	162.9	A	Inert
	12	149.6	B	Inert
	0.01	42.7	A	H_2
	0.01	43.0	A	H_2
	0.003	30.1	B	H_2
	0.003	26.2	B	H_2
	0.003	26.2	B	H_2

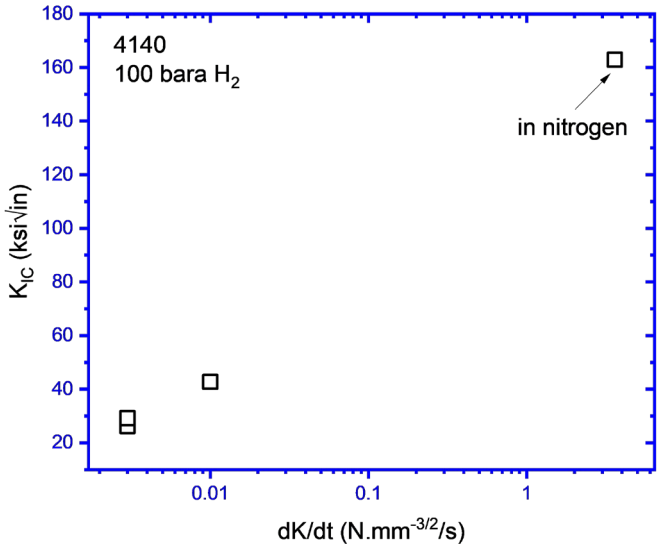

Figure 9—Comparing FT of 4140-110 in 100-bara H_2 vs. K Rate

5.3.2 Alloy 718-120 Results

The J-R curves for Alloy 718-120 are shown in Figures 10 and 11. The FT results for Alloy 718-120 from two labs are summarized in Table 7. The FT results obtained at each test lab are plotted as a function of the K rates and compared to the results obtained in the inert environments as well. The comparison is shown in Figure 12 for Alloy 718-120. The comparison clearly shows the significant reduction of the toughness in 100-bara H_2 compared to the inert environment. The toughness values also show clear dependency on the K rates at which the tests were performed. Lower toughness values were observed at lower K rates, as shown in both Table 7 and Figure 12.

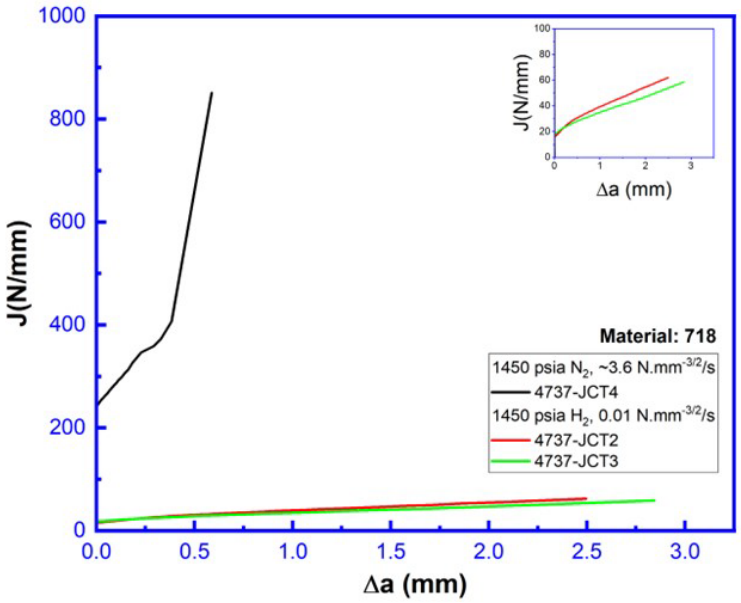

Figure 10—J-R Curves for Alloy 718-120 in Inert and H_2 from Lab A

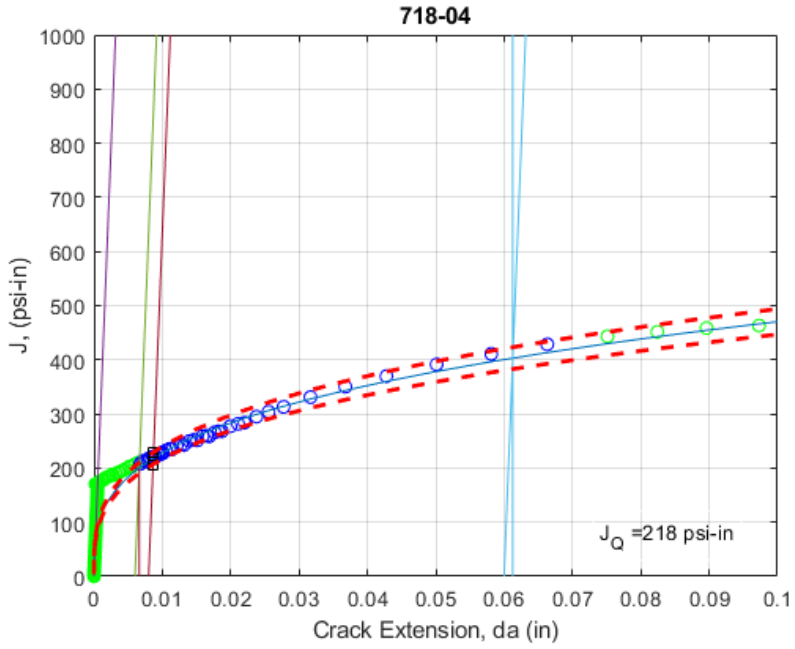

Figure 11—J-R Curves for Alloy 718-120 in H_2 from Lab B

Table 7—Summary of FT Results for Alloy 718-120

Grade	dK/dt ($N.mm^{3/2}.s^{-1}$)	J_{0mm} ($N.mm^{-1}$)	$J_{0.2mm}$ ($N.mm^{-1}$)	J_{1mm} ($N.mm^{-1}$)	K_{J0mm} ($ksi.in^{1/2}$)	$K_{J0.2mm}$ ($ksi.in^{1/2}$)	K_{J1mm} ($ksi.in^{1/2}$)	Test Lab	Env.
Alloy 718-120	3.8	240.4	246.4		210.6	213.2		A	Inert
	0.01	15.8	23.0	39.5	53.9	65.2	85.4	A	H_2
	0.01	18.1	23.4	35.2	57.8	65.6	85.6	A	H_2
Alloy 718-120	0.02	33.8	40.5	70.3	78.9	86.4	113.9	B	H_2
	0.02	31.3	38.2	61.4	76.0	83.9	106.4	B	H_2

NOTE J_{1mm} and K_{J1mm} was not obtained in the nitrogen test for 718-120 since the sample broke into two halves before reaching 1 mm crack extension. The AJ and β values thus were based on the regression of the data with crack extension shorter than 1 mm.

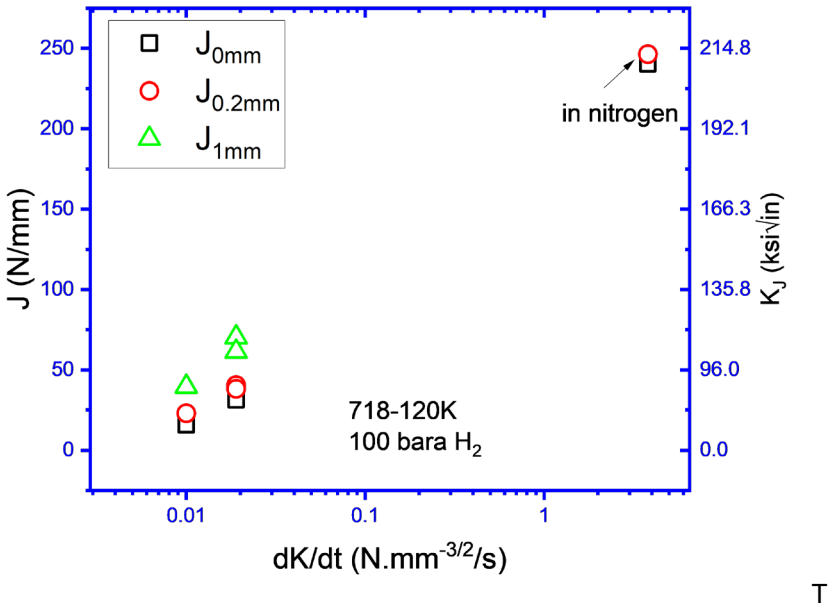

Figure 12—FT Results as Function of K Rates for Alloy 718-120 in 100-bara H_2

5.4 H_2 Permeation Results

5.4.1 4140-110

The H_2 flux experimental setup was validated by performing a H_2 permeation test using 3.5% sodium chloride (NaCl) (pH 8.2) on the charging side of the setup. A cathodic potential of -1050 mV vs. saturated calomel electrode (SCE) was applied to the sample on the charging side, which was an X52 line pipe steel. The oxidation side was the typical 0.1 M sodium hydroxide (NaOH) solution and was maintained at +300 mV vs. SCE. The purpose of this test was to make sure the use of a metal autoclave on the charging side, and the use of the fixtures mounting the sample to hold pressure, did not interfere with any H_2 uptake or the measurements. The flux transient from this validation test is shown in Figure 13. The red line is the numerical fitted line based on the solution to a one-dimensional diffusion and the symbols are the experimental data. As shown, the experimental data and the fitted line agreed very well and the effective diffusion coefficient of H_2 in the tested material was 9.4×10^{-8} $cm^2.s^{-1}$. The experimental results confirm that the experimental setup can measure the H_2 that diffuses through the sample.

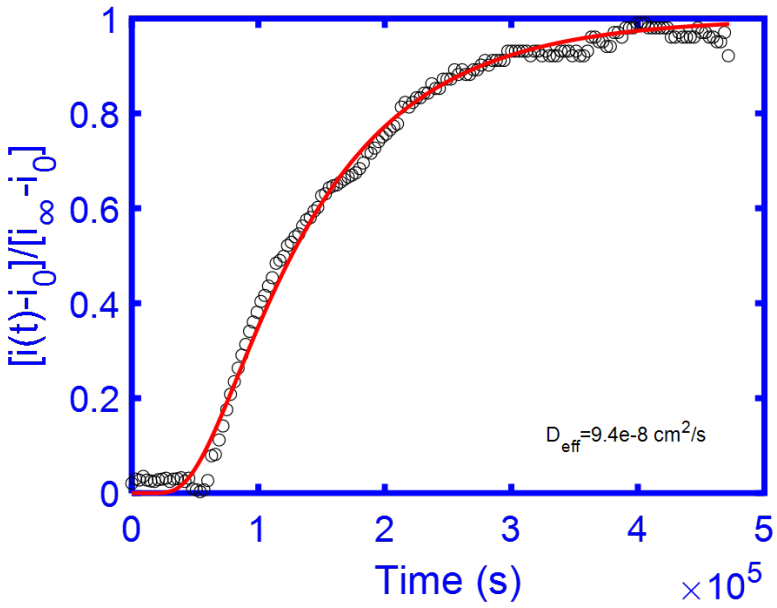

Figure 13—The Flux Transient as a Function of Time for the Test in 3.5% NaCl Solution at pH 8.2

Figure 14 shows the oxidation current as a function of time for the H_2 flux test that was performed for this project on 4140-110 steel sample. Prior to exposing the sample to H_2, a background current density about 12 nA.cm^{-2} was established on the oxidation side (exposed to 0.1 M NaOH and polarized to 0.3 V vs. SCE). H_2 pressure on the charging side was established. The measured current showed an increase at about 5.2 hours after the sample was exposed to high-pressure H_2, suggesting H_2 breaking through the sample and was detected on the oxidation side. The data were analyzed using the same method for the seawater under cathodic potential (SWCP) data based on the solution to a one-dimensional diffusion and compared in Figure 15. As shown, the experimental data agreed well with the fitted line and the effective diffusion coefficient in the tested material is 4.63x10^{-7} cm^2.s^{-1}.

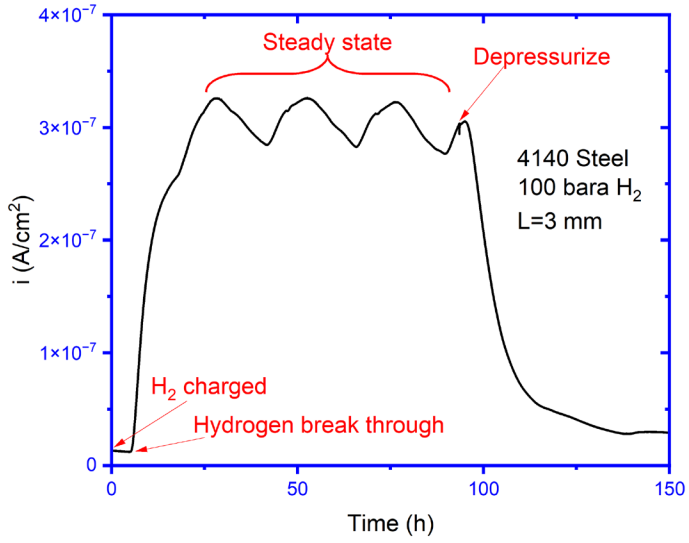

Figure 14—Current vs. Time Measured in the H_2 Flux Test with 4140-110 Steel in 100-bara H_2

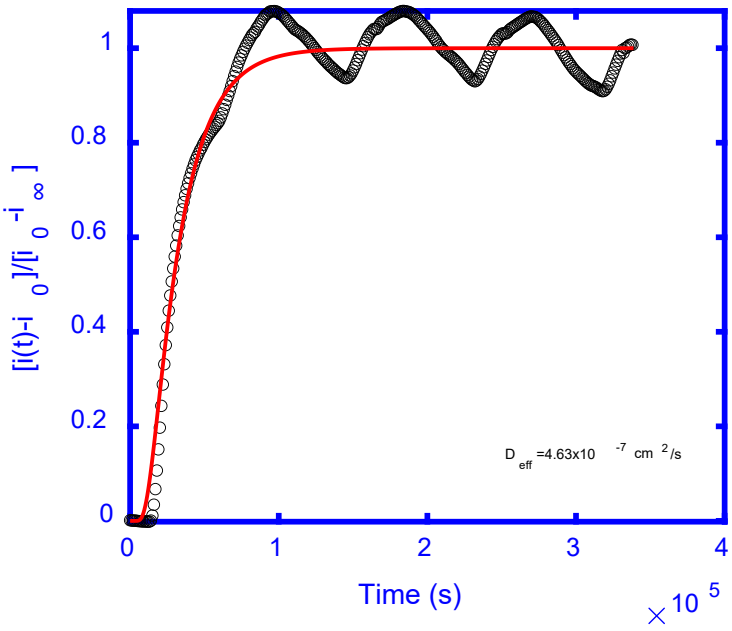

Figure 15—Flux Transient Measured in the Experiment (Symbols) and Theoretical Value (Red Curve) Comparison for the H_2 Flux Test with 4140-110 Steel in 100-bara H_2

Figure 16 shows the measured H_2 flux as a function of time. Using the steady-state H_2 flux and the derived effective H_2 diffusion coefficient. The subsurface H_2 concentration was calculated to be about 0.25 ppm.

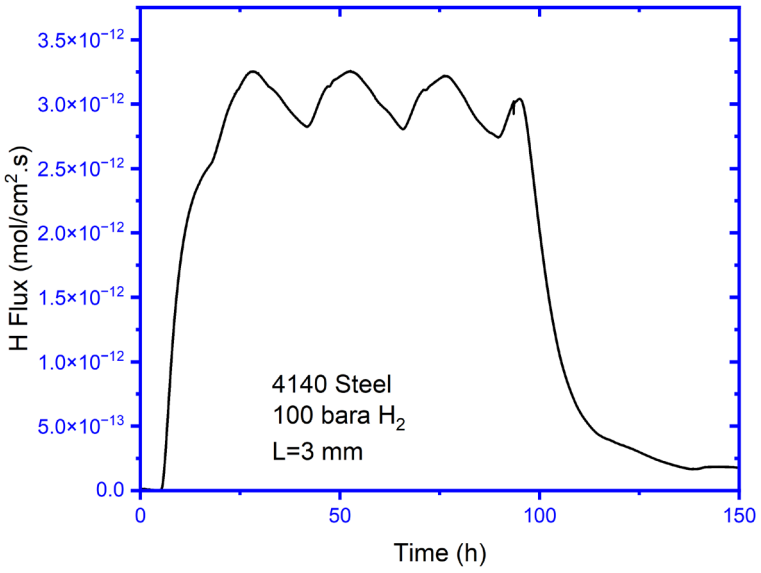

Figure 16—Measured H_2 Flux as a Function of Time for 4140-110 Steel Under 100-bara H_2

5.4.2 Alloy 718-120

The results for the permeation testing for 718-120 grade with 1450 psia H_2 gas are shown in Figure 17. The figure shows the permeation current density versus time. Low background currents were observed initially (nA range). The H_2 charging pressure was introduced at 30 hours after the solution in the oxidation cell was transferred. Testing was done for more than three weeks and no increase in the current was observed suggesting the lack of H_2 breaking through within the duration of testing. It should be noted that the sample thickness for this exposure was 0.118 in. (0.3 cm). Assuming that entry of H_2 was a not a limiting factor and a diffusion coefficient of $2x10^{-11}$ $cm^2.s^{-1}$ [14] for Alloy 718-120 at room temperature, the breakthrough time for a 0.3-cm-thick specimen would be on the order of 35 years. Use of a thinner sample could help in getting H_2 breakthrough in more reasonable test time but the challenge with a thinner sample (expected to be in micron thickness) would be whether it can be suitable for testing under high-pressure H_2 gas.

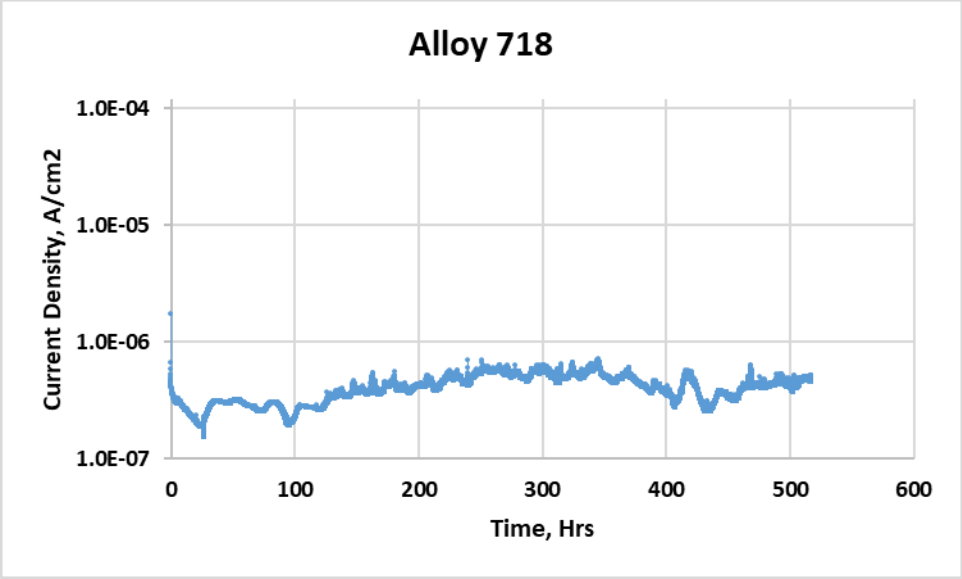

Figure 17—H_2 Permeation Measurements for the Alloy 718-120

6 Discussion

6.1 General

The results of the test program provide measures of susceptibility to HE for the materials tested. The results in H_2 for the two materials from the different test methods are used to understand the role of the test method and material type on the susceptibility to HE in high-pressure H_2.

6.2 Comparison of Materials

The SSR results for both materials showed a decrease in the plastic strain to failure and RA in high-pressure H_2 compared to inert environments. A comparison of the parameters from the SSR tests for both materials is shown in Figure 18.

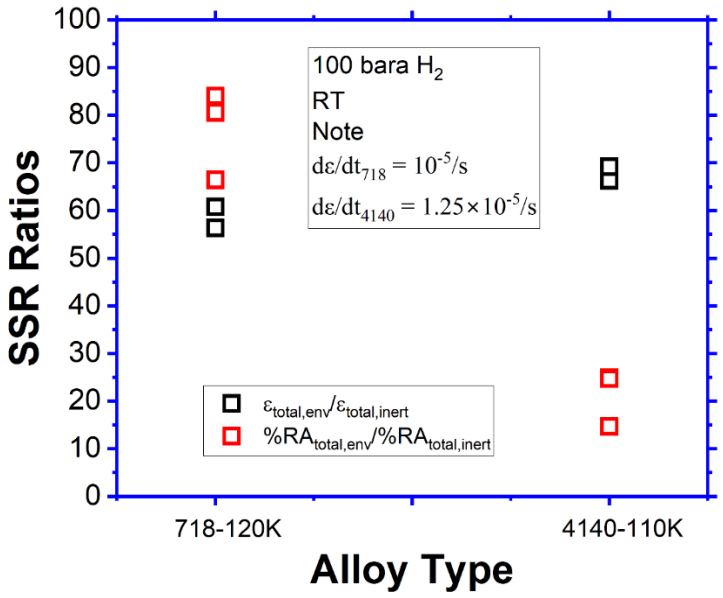

Figure 18—Comparison of the SSR Performances in 100-bara H_2 at RT

The comparison clearly suggests that the decrease in % RA (relative to the inert environment) for 4140-110 is significantly higher than for Alloy 718-120, even though the change in % total elongation (relative to the inert environment) is similar for both materials. Further SEM done on the fracture surfaces of the SSR specimens for both grades did show more brittle behavior in H_2 compared to their own performance in inert, but Alloy 718-120 showed some ductile features also present in the H_2 SSR specimen, while the 4140-110 H_2 SSR specimen did not show the same. The results suggest that even though the yield strength of the alloys is similar (~140 ksi), the responses in the SSR tests are very different, highlighting the difference between the alloy classes.

A comparison of the K_{th} values (as defined by J at the onset of crack extension) for the alloys is shown in Figure 19. The results clearly indicate that the K_{th} value of Alloy 718-120 is significantly higher than that of 4140-110 across the K rates tested, though it is possible that at very low K rates, the K_{th} value of Alloy 718-120 may be lower than the values measured at 0.01 $Nmm^{-3/2}.s^{-1}$ (the lowest K rate tested). In addition, to the higher values of K_{th}, Alloy 718-120 exhibited stable crack propagation, while 4140-110 exhibited unstable crack propagation. This indicates that not only was the K_{th} value of Alloy 718-120 higher but the crack growth rate was lower.

H_2 permeation studies at 100-bara H_2 showed that for 4140-110 steel, the effective diffusion coefficient was measured at $4.63x10^{-7}$ $cm^2.s^{-1}$. However, for Alloy 718-120, no H_2 breakthrough was possible, even after testing for weeks. 4140-110, which is Q&T low-alloy steel, has a martensitic microstructure, while Alloy 718-120 has an austenitic microstructure; diffusion of H_2 through a martensitic microstructure is faster than in an austenitic microstructure [13].

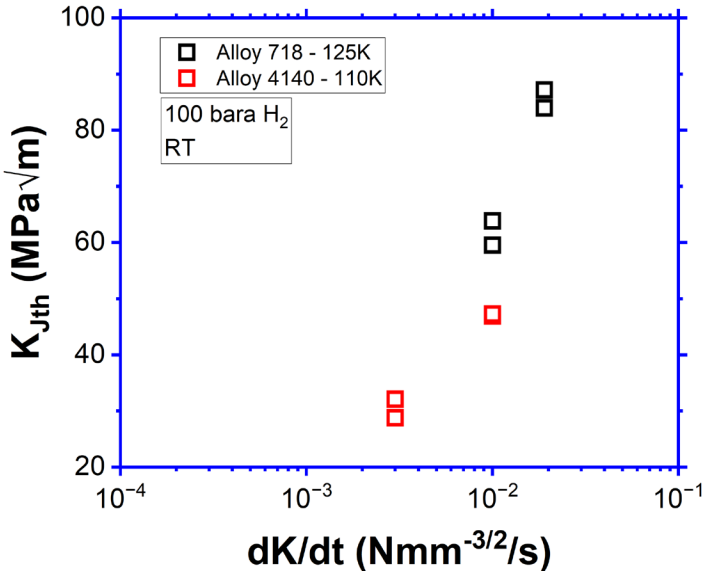

Figure 19—Comparison of the K_{th} Values of the Two Alloys Tested in 100-bara H_2 at RT

6.3 Influence of Loading Parameters

The FT results show that the FT values of the materials are sensitive to the tested K rate. In the current work among the K rates tested for both materials, no plateau in K_{th} values was observed. It should be noted some of the differences in K_{th} values at different K rates may be attributed to the tests at different K rates being performed at different laboratories.

In order to better understand the effect of K rates, one of the labs performed an additional test at constant K conditions. The procedure to establish constant K conditions was based on work performed by the lab internally for other projects. The results of the constant K tests at 49.5 MPa.m$^{1/2}$ is shown in Figure 20. A very slow static crack growth rate (SCGR) of 2x10^{-9} mm.s^{-1} appears to be evident under constant K conditions.

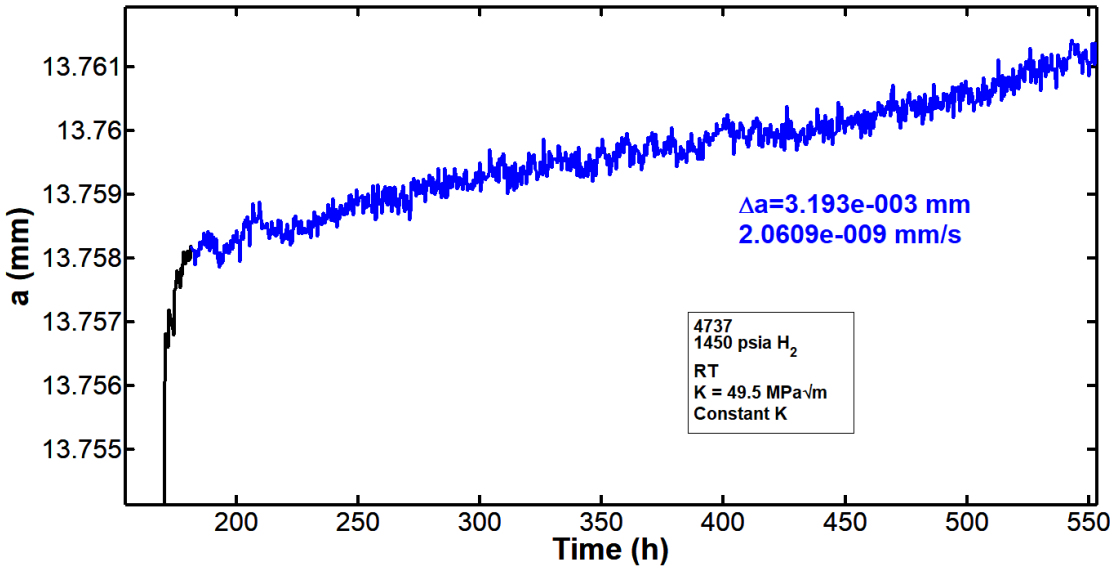

Figure 20—Crack Growth Rate under Constant K Conditions (K=49.5 MPa.m$^{1/2}$) for Alloy 718-120

The SCGR at 60.5 MPa.m$^{1/2}$ under constant K conditions is shown in Figure 21. The SCGR is about 2.6´10^{-6} mm.s^{-1}, a 1,000-fold increase from the SCGR at 49.5 MPa.m$^{1/2}$, suggesting that the K_{th} could be around 49.5 MPa.m$^{1/2}$ under constant K or very low K rate conditions.

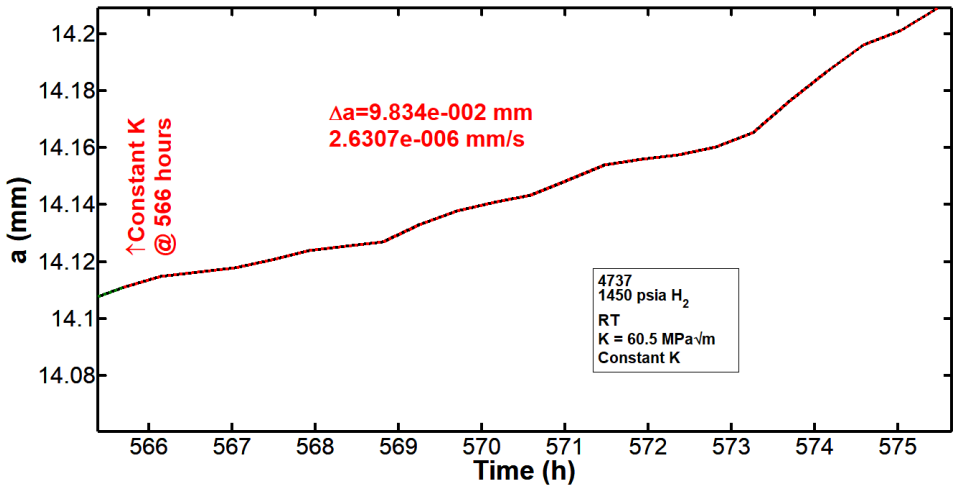

Figure 21—Crack Growth Rate under Constant K Conditions (K=60.5 MPa.m$^{1/2}$) for Alloy 718-120

The results of the constant K tests performed further help understand the role of K rates on the K_{th} behavior of Alloy 718-120 in high-pressure H_2. A summary of the effect of K rate on the measured K_{th} for Alloy 718-120 is shown in Figure 22. These results indicate that for Alloy 718-120 under these conditions, the constant K conditions appear to provide lower K_{th} values than the K rates used for testing in this program. It is possible that slow rising displacement at K rates of 0.005 Nmm$^{-3/2}$.s^{-1} or less (lower than used in this test program) may provide a sufficiently low K rate to provide lower bound values of K_{th} and that low K rates for FT testing in general (while ensuring practicality of the tests) could be used to obtain more conservative FT values for materials.

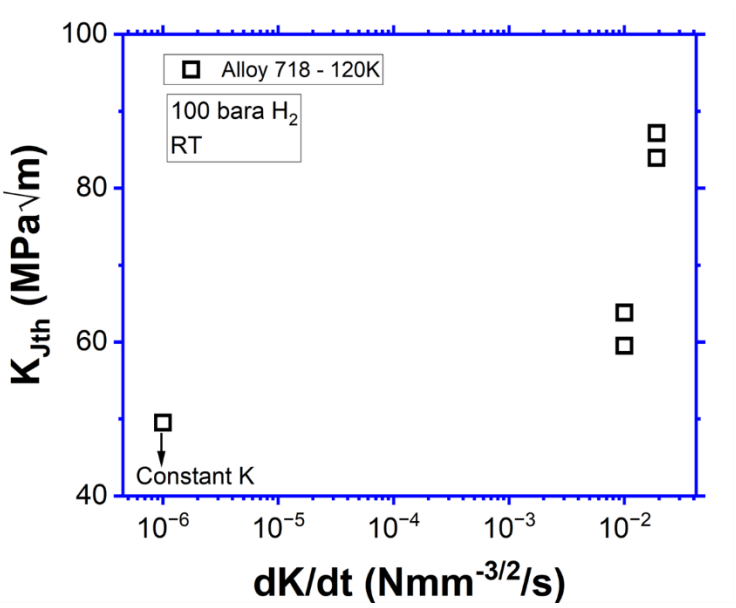

Figure 22—Effect of K Rate on the K_{th} Behavior of Alloy 718-120 in 100-bara H_2 at RT

6.4 Summary

Overall, the test program demonstrated that metallic materials could experience reduction in ductility and toughness under high-pressure H_2 that can be relevant to underground storage applications compared to inert behavior of the same material. Additionally, materials with similar yield strength but different microstructure have different retained ductility and FT values. Currently, no specific acceptance criteria or qualification test method exists for choosing materials in these applications. The intent of this test program was to obtain data using relevant test methods while using the learnings of current program as input into future ones. One of the inputs for future test programs that can be relevant is using a lower K rate for FT testing of metallic materials to further refine FT values of materials in high-pressure H_2.

Annex A
(informative)

Experimental Details for API Material Testing in H_2 from Lab A

A.1 Test Materials and Specimens

A.1.1 Materials

The materials tested in the project were provided by API. The provided Alloy 718-120 and 4140-110 grades were assigned Lab A identification numbers (IDs) of 4737 and 4738. Both materials were provided as a bar form 12 in. in length and 5 in. in OD for Alloy 718-120, and 17 in. in length and 5 in. in OD for 4140-110 steel. Longer material was provided for 4140-110 steel due to the need of machining SSR samples and flux samples. Table A.1 shows a summary of the material dimensions and the mechanical properties.

Table A.1—Dimensions and Mechanical Properties of Supplied Materials

Grade	Lab A ID	Diameter (in.)	Length (in.)	Yield Strength (ksi)	Tensile Strength (ksi)
Alloy 718-120	4737	5	12	135.2	181.8
4140-110	4738	5	17	137.0	154.4

A.1.2 Specimen Description

A.1.2.1 SSR Specimen

SSR tests were performed for 4140-110 grade using the button head SSR samples. An example schematic of the button head SSR sample is shown in Figure A.1. SSR samples were also extracted from the mid-radius location of the bar.

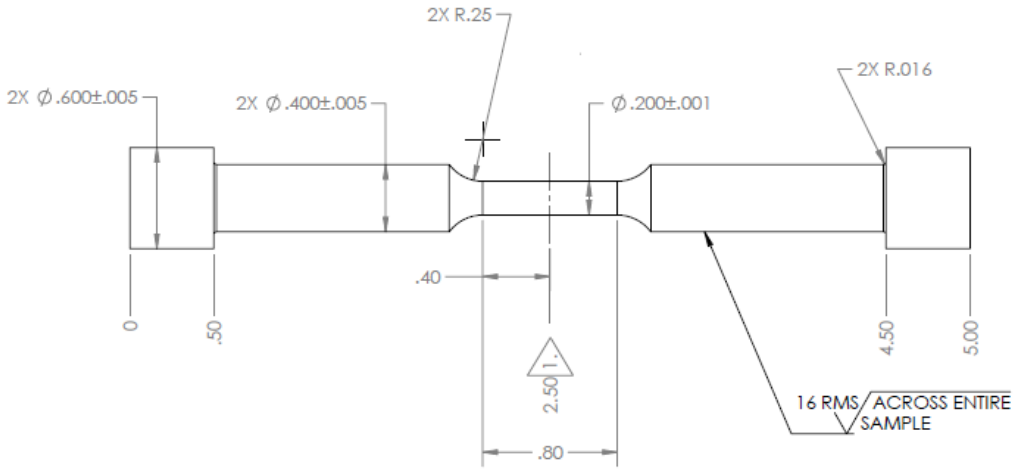

Figure A.1—Schematic of the Button Head SSR Sample

A.1.2.2 FT Specimen

Compact tension [C(T)] specimens were used to perform FT testing and were extracted from the provided materials at the mid-radius location (Figure A.2). The samples were notched in the C-L orientation as per ASTM E1823, with the crack growing along the longitudinal direction of the bar.

A schematic of the C(T) FT specimen is shown in Figure A.2. The samples were machined to the following dimensions:

— Specimen width, W=1″ (1.25 in.)

— Specimen thickness, B=0.5″ (0.3 in.)

— Initial a/W=0.5 (where a is the total crack length including the pre-crack. Nominal notch depth 0.45 in. with 0.05-in. pre-cracking in air) (0.5)

— Specimens were side-grooved by 5% of the thickness on each side. The samples were side-grooved prior to pre-cracking. (side-grooved similarly)

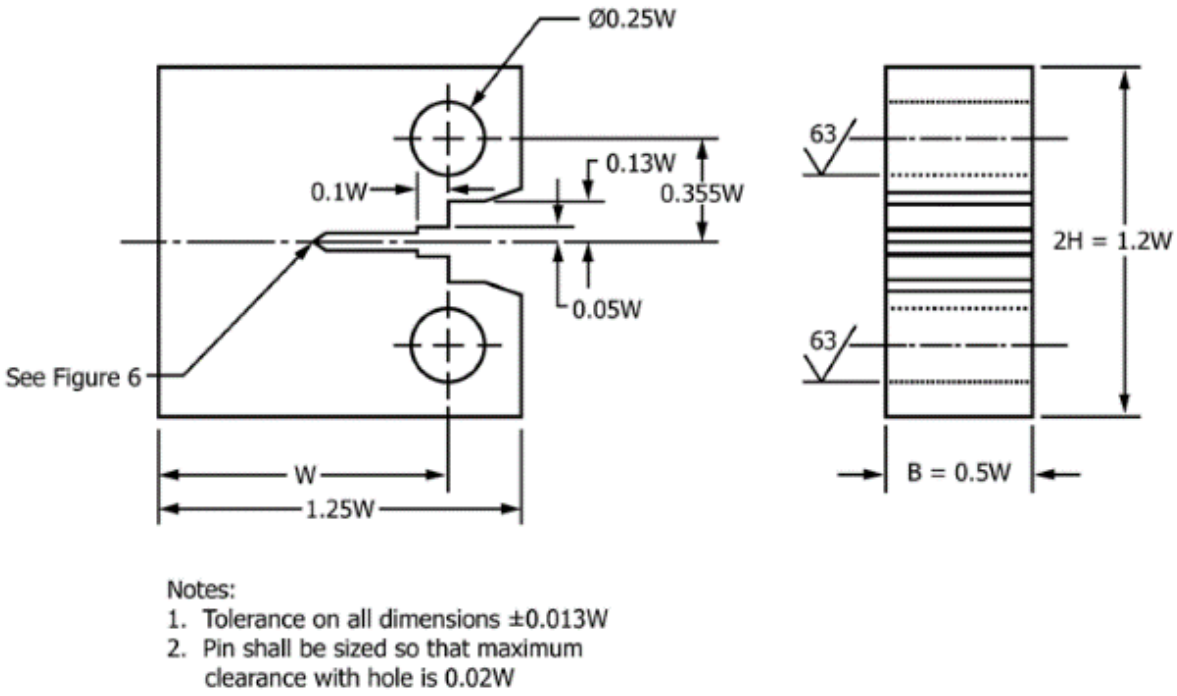

Figure A.2—Schematic of the FT C(T) Specimens (Ref: ASTM E1820)

The samples were pre-cracked in air to an initial a/W of 0.5 under a constant K_{max} of 25 ksi√in (27.5 MPa√m) with R rations varying from 0.2 to 0.4 and at 2 Hz. The last 15 mils of the pre-cracking were performed under a ΔK of 15 ksi√in (16.5 MPa√m). All pre-cracking was done at Lab A.

A.1.2.3 H_2 Permeation Specimen

A disk sample with 3-mm thickness was used in H_2 flux test, as shown in Figure A.3.

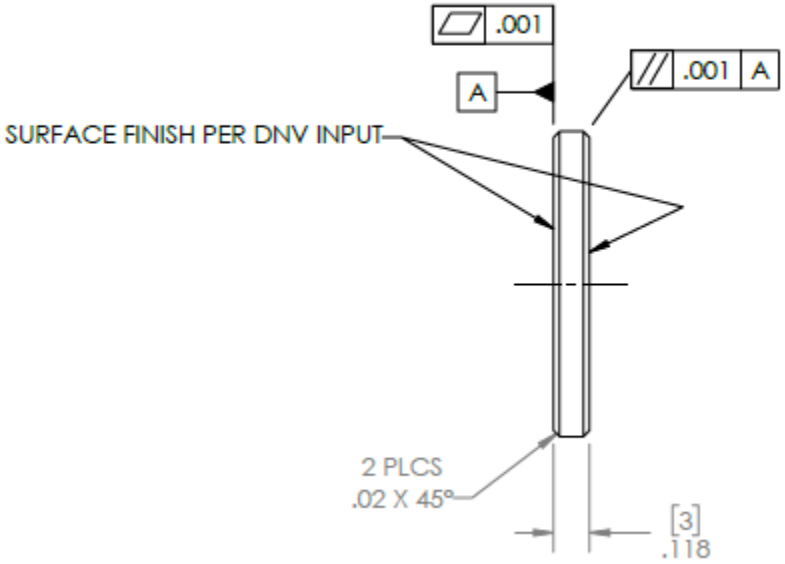

Figure A.3—Dimensions of the H_2 Permeation Sample

A.2 Test Matrix

Table A.2 lists the tests that were performed in the project, including the FT tests, SSR tests, and the H_2 flux test.

Table A.2—Test Matrix

Material	Type of Testing	Environment	Number of Tests
Lab A ID 4737 (Alloy 718-120)	FT	100-bar N_2	1
		100-bara H_2, measure O_2 and moisture	2
Lab A ID 4738 (4140-110)	FT	100-bar N_2	1
		100-bara H_2, measure O_2 and moisture	2
	SSR	100-bar N_2	3
		100-bara H_2, measure O_2 and moisture	3
	H flux	100-bara H_2, measure O_2 and moisture	1

A.3 Test Details

The tests in this project were performed using 100% H_2 to study the environmental effect and in N_2 to establish the baseline performance in an inert environment. All tests were performed at a total pressure of 100 bar and at RT.

A.3.1 Environmental Testing Procedure

All environmental tests were performed in Alloy C276 (nickel-based alloy) autoclaves. The test specimens were electrically isolated from the autoclave, and the test frame, to prevent ground loops affecting the crack growth measurements. The autoclaves were assembled with the test specimen to be tested, sealed, and pressure-tested overnight at 2000 psig. After the pressure test, the autoclave/sample was purged with high-purity N_2 overnight to reduce moisture. This was followed by cycles of 150 psig N_2 and vacuum to remove N_2 from the previous step. This pressure-release cycle was repeated five more times to minimize O_2 in the system. This was followed by pressurization of the autoclave with test gas, 100% H_2 to 150 psig and vacuuming out the filled H_2. This pressure-release cycle was repeated one more time. This step was followed by flowing the test gas through the autoclave at a pressure of 500 psig at a flow rate of about 0.5 standard cubic feet per hour (SCFH). The gas outlet from the autoclave was connected to an O_2 analyzer. The lines connecting the sensor to the autoclave were also preconditioned using the N_2/vacuum and H_2/vacuum cycles. Once the O_2 concentration reached less than 1 ppm, the autoclave was pressurized to 100 bar and all valves connecting to gas tanks were closed. Along with the O_2 sensor, there was a moisture analyzer connected to the autoclave to confirm that the moisture was low enough to validate all results obtained. The system was allowed to stabilize for at least 2 hours before loading the sample at the displacement rate. At the conclusion of the test, the pressure of the autoclave was brought down to ambient by releasing the gas through the O_2 analyzer to ensure that the O_2 stayed less than 1 ppm during the test.

A.3.2 SSR Testing

SSR tests were performed using servo electric frames which record the load and displacement of the testing samples. All samples were strained until failure. The SSR testing was done at strain rate of $1.25x10^{-5}$ s^{-1}.

Upon completing the SSR tests, all specimens were removed from the test vessel and the diameter of the sample near the fracture location was measured using a stereomicroscope. This value was used to calculate the RA. The samples were also examined to document any indication of brittle failure or secondary cracking.

A.3.3 FT Testing

The setup is shown in Figure A.4 used for FT using slow rising displacement method. The inert tests in N_2 were performed at a displacement rate of 1x10-4 $in.s^{-1}$ corresponding to a K rate of 3 to 4 $N.mm^{-3/2}.s^{-1}$. The tests in N_2 not only help establish the baseline performance of the materials in an inert environment but also help establish the displacement rate that is required to achieve the K rate for the tests in H_2. FT tests in H_2 performed under displacement control at a low initial K rate of 0.01 $N.mm^{-3/2}.s^{-1}$ to capture the environmental effect. The crack length in all tests were measured in situ using the direct current potential drop (DCPD) technique. A constant current of 4 amp was used for DCPD crack length monitoring and the voltage drop across the crack mouth was measured using a high resolution digital multi-meter. The polarity of the current was frequently alternated during each DCPD datapoint measurement. This was done to eliminate thermal junction potentials in the system and improve the accuracy of DCPD. Ni wires encased in polytetrafluoroethylene (PTFE) heat shrink sleeves were used for the current and voltage signals. The spot weld locations of the probes on the samples were coated (using proprietary epoxy) as a strain relief. The measured voltage drop was converted into crack length using the Johnson equation (Equation A1.2 in ASTM E1457). The voltage drops, as well as the converted crack length, were recorded using a proprietary software program. Upon completing the FT tests, all specimens were removed from the autoclaves and broken open to examine the fracture surface using a stereomicroscope for measurement of the actual initial and final crack length.

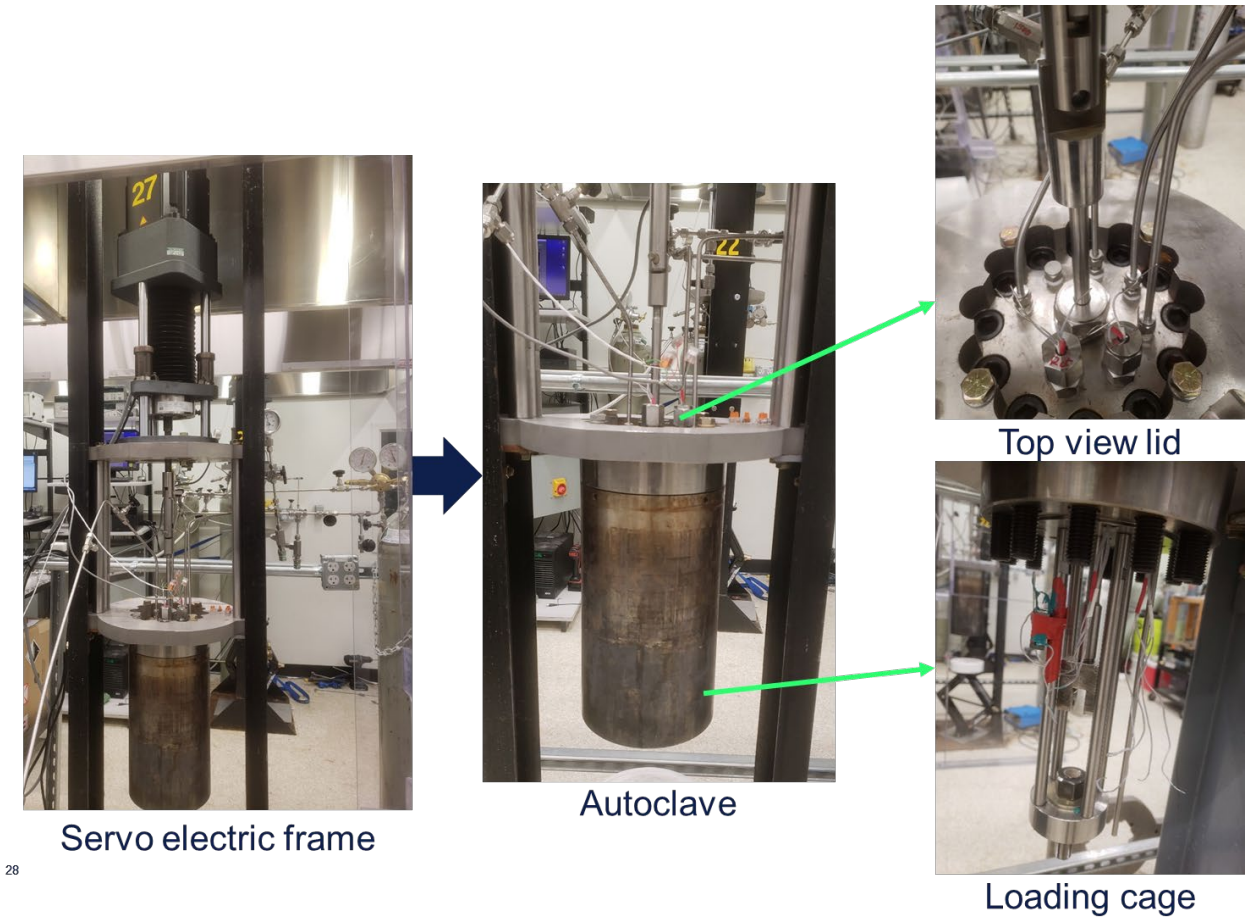

Figure A.4—Test Setup Showing the Test Frame, Autoclave, and the Gas Cylinders

A.3.4 H_2 Flux Measurement

H_2 flux measurement for permeation was performed using the Devanathan-Stachurski cell technique and the instructions described in ASTM G148. The experimental setup is shown in Figure A.5. The experimental setup consists of a C276 autoclave on the H_2 charging side and an acrylic cell on the oxidation side. The oxidation side of the 4140-110 sample was coated with electroless nickel plating.

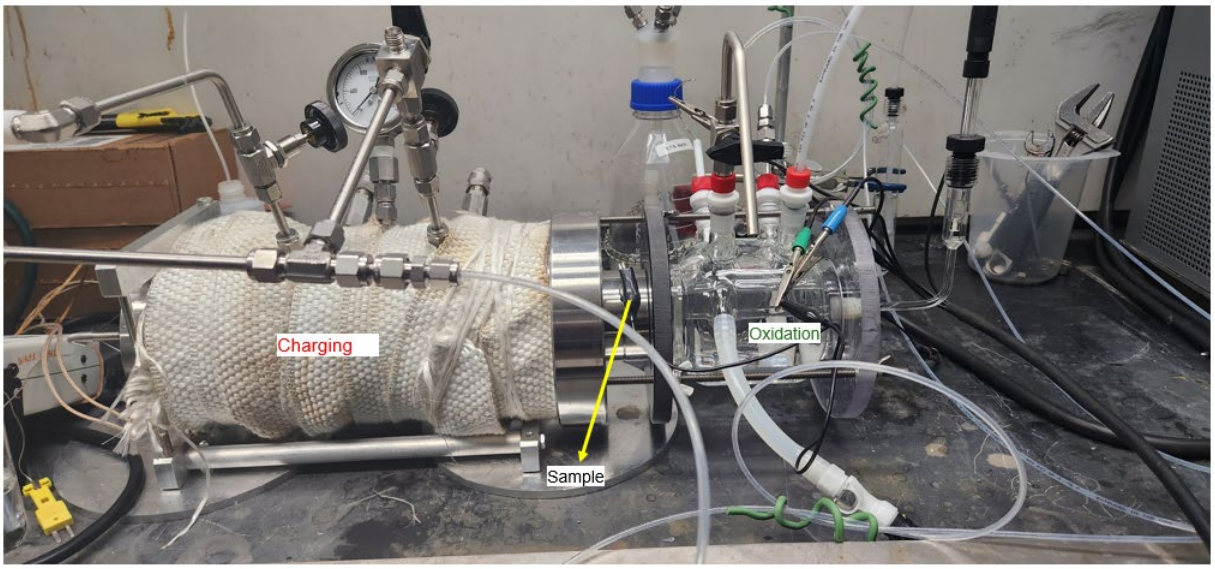

Figure A.5—H_2 Flux Experimental Setup

The oxidation cell contains 0.1 M NaOH solution that is constantly purged using high-purity N_2. A Pt/Nb wire loop and a SCE, were used as counter and SCE reference electrodes, respectively.

Prior to starting the test, the NaOH solution and the oxidation cell were both deaerated with high-purity N_2 overnight. Once the solution and the cell were fully deaerated, the solution was transferred to the oxidation cell under N_2 pressure to avoid any O_2 ingress into the oxidation cell. The sample then was polarized to 0.3 V vs. SCE while the current was measured to establish a steady background. Typically, a background current density lower than 100 nA/cm^2 is expected. After the background current density fell to less than 100 nA/cm^2, the autoclave was subjected to the same charging procedure as that used in the FT testing and SSR testing. This provided low O_2 and moisture conditions on the charging side and to establish 100-bara H_2 pressure to begin H_2 flux measurement. Constant applied potential on the oxidation side would facilitate oxidation of any H_2 diffusing through the sample from the charging side. When H_2 diffuses through the testing sample, this would result in a current transient, i.e., current increasing and then reaching a plateau, that could be used to convert to diffusion flux and calculate the H_2 diffusion coefficient.

A.4 Data Analysis

A.4.1 SSR Data Analysis

SSR data were analyzed to determine the various parameters such as TTF, % Plastic Elongation, % Reduction of Area etc. in accordance with the instructions in NACE TM0198, ASTM G142.

A.4.2 FT Data Analysis

The data from the FT tests were analyzed using ASTM E1820. The FT value of J was calculated from the sum of the elastic and plastic components according to equations (1) through (3) below:

$$J_{tot} = J_{el} + J_{pl} \tag{1}$$

$$J_{tot} = \frac{K_{(i)}{}^2 (1-\upsilon^2)}{E} + J_{pl(i)} \tag{2}$$

$$J_{pl(i)} = \left[J_{pl(i-1)} + \left(\frac{h_{pl(i-1)}}{b_{(i-1)}} \right) \frac{A_{pl(i)} - A_{pl(i-1)}}{B_N} \right] \left[1 - g_{(i-1)} \left(\frac{a_{(i)} - a_{(i-1)}}{b_{i-1}} \right) \right] \quad (3)$$

where

i step;

K stress intensity factor ($N \cdot mm^{-3/2}$);

$$K = \frac{P}{(BB_N W)^{1/2}} f\left(\frac{a}{W}\right)$$

P load (N);

υ Poisson's Ratio, 0.32;

E Young's Modulus (MPa): assumed to be 200138 MPa (29000 ksi);

$$\eta_{pl(i-1)} = 2 + 0.522 b_{(i-1)} / W$$

$$\gamma_{pl(i-1)} = 1 + 0.76 b_{(i-1)} / W$$

A_{pl} plastic component of the area under the Load CMOD curve (based on ASTM E1820 A2.4.2.2, equations A2.9, A2.10, and A2.11);

B sample thickness (mm);

B_N sample thickness at the root of side grooves (mm);

W sample width (mm);

a crack length (mm); and

b remaining ligament (mm), *W-a*.

The processed J vs. Δa was fitted to Equation (4):

$$J = A_J \Delta a^{\beta} \quad (4)$$

The fitting parameters, J at 0 mm (point of first crack extension), 0.2 mm and 1 mm of crack extension and the J value at the maximum load are reported. The value $J_{maxload}$ is derived at the maximum force. These J values were also converted to K_J using Equation (5):

$$K_J = \sqrt{\frac{JE}{1 - \nu^2}} \quad (5)$$

A.4.3 H_2 Flux Data Analysis

In the case H_2 diffusion does occur, and H_2 oxidation current is measured, the rising transient of the sample can be expressed by the following equation:

$$\frac{i_t - i_0}{i_\infty - i_0} = \frac{2L}{\sqrt{\pi Dt}} \Sigma_{n=0}^{\infty} \exp\left(-\frac{(2n+1)^2 L^2}{4Dt} \right) \tag{6}$$

where

i_t transient current at time t (A/cm^2);

i_0 initial current at t=0 (A/cm^2);

i_∞ steady-state current at t→∞;

L sample thickness (cm);

t time (s); and

D diffusion coefficient (cm^2/s).

A script from a proprietary software package was used to do a regression and generate flux data and calculate the diffusion coefficient.

The measured current can be converted to H_2 flux using the following equation:

$$J = \frac{i}{F} \tag{7}$$

where

J H_2 flux (mol/cm^{2}s);

i current density (A/cm^2); and

F Faraday constant (96485 c/mol).

The subsurface H_2 concentration can be calculated using the following equation:

$$C_0 = \frac{J_{SS} L}{D_{eff}} \tag{8}$$

where

C_0 subsurface H_2 concentration (mol/cm^3);

J_{SS} steady-state H_2 flux (mol/cm^2.s);

L flux specimen thickness (cm);

D_{eff} effective H_2 diffusive coefficient (cm^2/s.)

Annex B
(informative)

Experimental Details for API Material Testing in H_2 from Lab B

B.1 Materials and Specimen Geometries

Two material grades were provided for evaluation in low-alloy steel 4140-110 quenched and tempered to 110 ksi minimum yield strength (MY) and Alloy 718-120 per API 6ACRA were provided. The materials were nominally 5 in. in diameter and sufficient quantifies were provided to fabricate all necessary specimens and spares. The material forms and nominal tensile properties as provided in the material test reports are provided in Table B.1.

Table B.1—Material Forms and Tensile Properties from Material Testing Reports Provided by API

Grade	Form	0.2% Yield Stress (ksi)	UTS (ksi)	Elongation (%)	RA (%)
4140-110	5-in. round	142.1	157.9	18.9	57.9
Alloy 718-120	5-in. round	135.2	181.8	27.6	40.2

All test specimens were excised at the mid-radius. The SSR tensile bars were oriented in the longitudinal (axial) direction and FT specimens were oriented in the transverse direction with C-L notch orientation. Test specimens were fabricated as outlined in ASTM G142 for SSR as shown in Figure B.1.

Two different C(T) specimen geometries per ASTM E1820 were utilized for the FT testing. The air specimens were larger due to a higher anticipated FT in the absence of H_2 (width, W, equal to 2 in. and thickness, B, equal to 1 in.) as shown in Figure B.2. This larger specimen ensured valid test results and J-dominance. The H_2 test specimens were fabricated to be compatible with existing autoclave hardware (W of 1.25 in. and B of 0.30 in.) as shown in Figure B.3. After fatigue pre-cracking, the specimens were side-grooved nominally 20% total in the thickness dimension (10% on each side).

A permeation membrane was machined from the Alloy 718-120 for permeation studies. The sample was removed from mid-radius location. The rectangular membrane had dimensions of 1.55 in. width, 1.76 in. length, and was 0.118 in. (3 mm) in thickness as seen in Figure B.4. The one side that would be exposed to the oxidation cell (detection side) was coated with palladium (Pd) prior to testing.

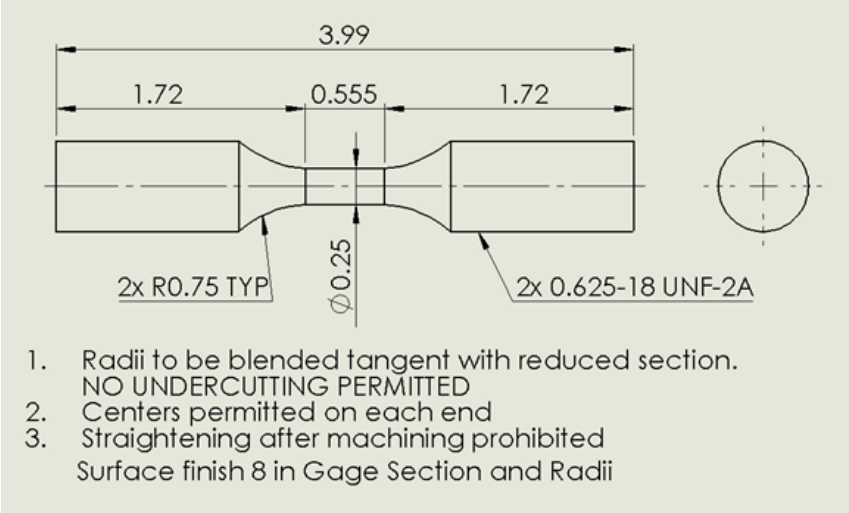

Figure B.1—SSR Specimen Geometry

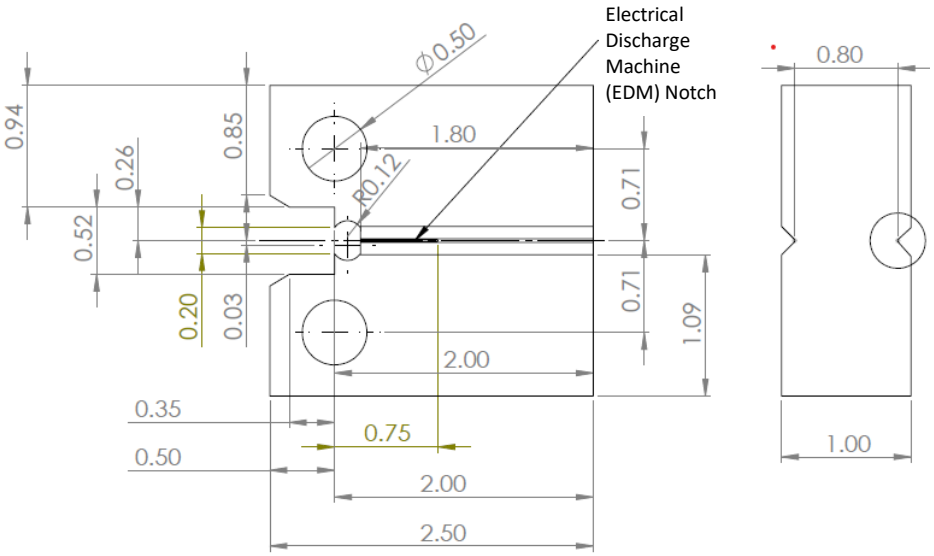

Figure B.2—C(T) Specimen Geometry for Baseline Air FT

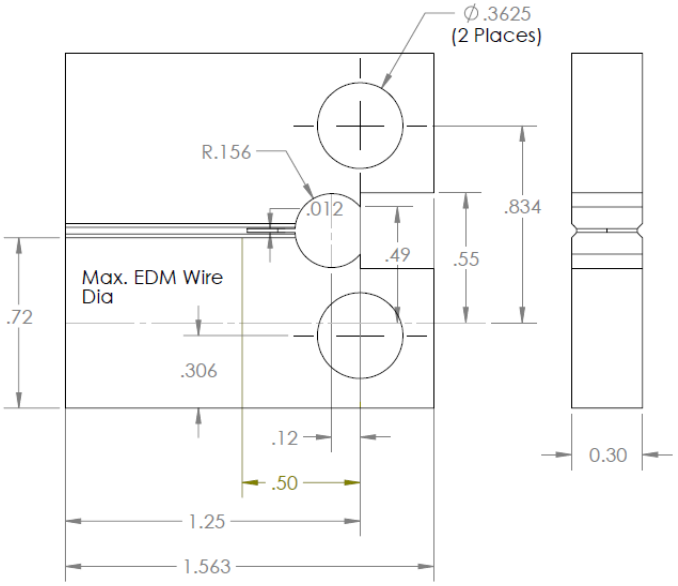

Figure B.3—C(T) Specimen Geometry for FT Tests in H_2 Environment

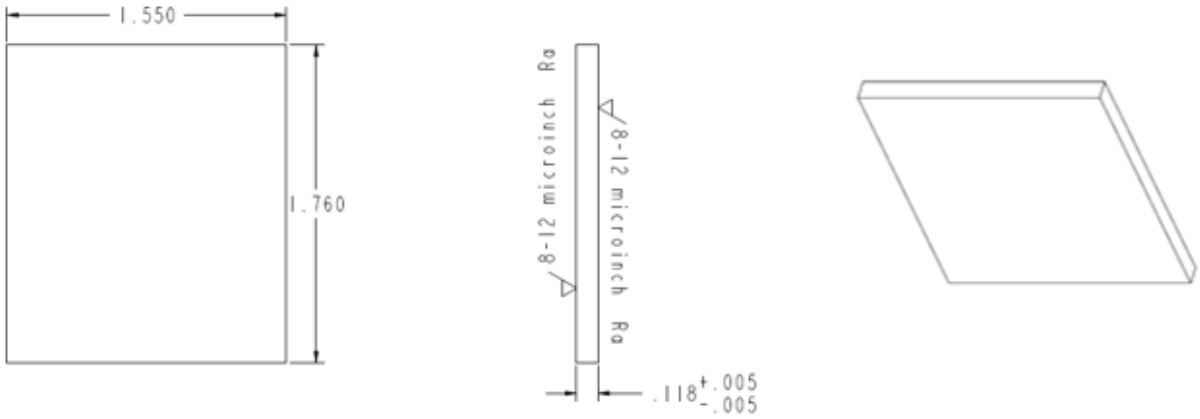

Figure B.4—Schematic of Sample Used for H_2 Permeation Studies

B.2 Test Methods

In this testing program, SSR, FT, and permeation tests were performed. The SSR testing was performed on Alloy 718-120 only in 100-bara H_2 and 100-bara He (inert) environments. The FT testing was performed in air and 100-bara H_2 gas on 4140-110 and Alloy 718-120. The permeation testing was performed on Alloy 718-120 only. High-purity H_2 gas (99.999%) was utilized for all H_2 testing. The following sections describe the test methods for the identified tests.

B.2.1 SSR Testing

SSR testing in 100-bara He (inert) and 100-bara H_2 gas environments was performed in accordance with ASTM G142. This testing utilized a servo-hydraulic test frame outfitted with an autoclave for high-pressure high temperature H_2 gas testing. Tests were controlled at a constant actuator displacement rate to achieve a target strain rate of 1×10^{-5} s^{-1}, and test data were collected from each test with a proprietary-software-based data acquisition system. The gauge section displacement was measured in situ using an extensometer, and strain was calculated from this local displacement measurement. For each test, the

load, pressure, extensometer, and actuator linear variable differential transformer (LVDT) displacements were continuously collected. The autoclave preparation followed standard lab procedures for ensuring gas quality, as previously described.

Stress-strain curves were developed for each test, and the following tensile test parameters were determined: 0.2% yield stress, the ultimate tensile stress, % elongation (both total, plastic), TTF, % RA, etc. The elongation was determined from gauge marks scribed on the specimen before testing, and after testing this distance was measured using a traveling microscope and compared to the initial distance. The reduction of area was calculated from the minimum diameter of each specimen after testing and the specimen diameter before testing. The inert (He) test data were compared to the gaseous H_2 data.

B.2.2 FT Testing

The objective of this task was to apply the test method E1820 to measure the crack initiation toughness (J or K_J) and cracking resistance curves (J-R curves) of each material in air and 100-bara H_2 gas. Test specimens were fabricated per the cut plan and specimen drawings and then fatigue pre-cracked in lab air. After pre-cracking, specimens were side-grooved to nominally 20% (10% each side). For the H_2 gas tests, specimens were not pre-charged or presoaked, and testing was started as soon as steady-state conditions (temperature and pressure) were achieved in the autoclave. The crack initiation toughness and cracking resistance curves were measured on duplicate specimens for each material in 100-bara H_2 gas. In addition to these H_2 gas tests, test method E1820 was performed on at least one specimen for each material in lab ambient conditions to determine the baseline crack initiation toughness and J-R behavior.

The elastic-plastic fracture mechanics methods in ASTM E1820 were utilized to measure fracture initiation toughness and crack growth resistance. The anticipated FT values (J_{IC}) from the technical literature were used with the yield stress of each material to determine the minimum specimen thickness (B) and remaining ligament length determined by the specimen width and crack length (a) to ensure J-dominance and valid toughness results.

$$W - a, B > 10 J_Q / \sigma_Y$$

Integral knife edges were fabricated into the specimens to measure the load-line crack-opening displacement (COD) throughout each test. Integral knife edges allowed secure attachment of COD or clip gauges to the test specimens. Following fabrication, the specimens were polished in and around the crack extension zone, and a lab datasheet was created to document test specimen dimensions and subsequent test steps. After pre-cracking and side-grooving, the H_2 gas tests were instrumented with DCPD probes to measure the in situ crack extension.

The H_2 gas tests were performed in autoclaves coupled to servo-hydraulic test frames. The test specimens were placed into the load train, and the DCPD wires were fed through ports in the autoclave head. The COD gauge was attached, and DCPD probes were connected to the test system. The system was sealed, leak-checked using high-pressure N_2 gas, and then purged using standard operating procedures. To ensure gas purity in the test autoclave, the autoclave was placed under vacuum, and a series of N_2 gas and H_2 gas purges were performed. The autoclave was then pressurized with high-purity H_2 gas to the prescribed testing pressure. These procedures have been verified with gas sampling to achieve less than 1 ppm O_2 and less than 5 ppm H_2O. As prescribed in ASTM E1820, tests were performed under actuator displacement control at a constant rate. The displacement rate was calculated based on specimen dimensions and compliance to achieve a target initial K rate of 1 MPa√m per hour (or 0.91 ksi√in. per hour).

For the air tests, the unloading compliance method was utilized to infer crack length from the specimen compliance by periodically unloading the specimens during the tests, and for the H_2 gas tests, the crack length was measured using DCPD as outlined in ASTM E1820, Annex 18, and periodic unloads were not used to infer crack length. The air tests were controlled and post-test analyzed using Fracture Technology Associates (FTA) software and hardware. This software automates the periodic unloading segments and

accurately controls the test. The FTA software has an integrated software package for post-test analysis to develop J-R curves, identify the cracking initiation toughness (J_Q), and determine if validity requirements were satisfied.

For the H_2 gas tests, load, COD, and DCPD voltage (converted to crack length) were continuously measured throughout each test using a proprietary-software-based data acquisition system. Based on these data, the J versus crack extension (Δa) curves were constructed using a script from a proprietary software package following procedures specified in ASTM E1820. The crack length was calculated per a linear transformation from DCPD voltage and not as outlined in Annex 18 of the standard. From this construction, the crack initiation toughness (J_Q) was identified, and all validity criteria were evaluated.

B.2.3 H_2 Permeation Testing at High Pressure

H_2 permeation testing was performed in a specialized stainless-steel high-pressure autoclave test apparatus. Testing was performed using an electrochemical technique per ASTM G148. This assembly, which is shown in Figure B.5 has two chambers: a charging side with the high-pressure gaseous environment and an oxidation side where the H_2 permeating through the sample is measured. The holder was fabricated to adjust the exposed area considering the strength of the material, thickness of the membrane, and test pressure. For Alloy 718; the machined and Pd-coated membrane on one side was placed in the holder in between two stainless steel plates. A seal is created by tightening the plates between the flanged ends. The charging side was then thoroughly deaerated and pressure checked prior to testing using 100% He gas.

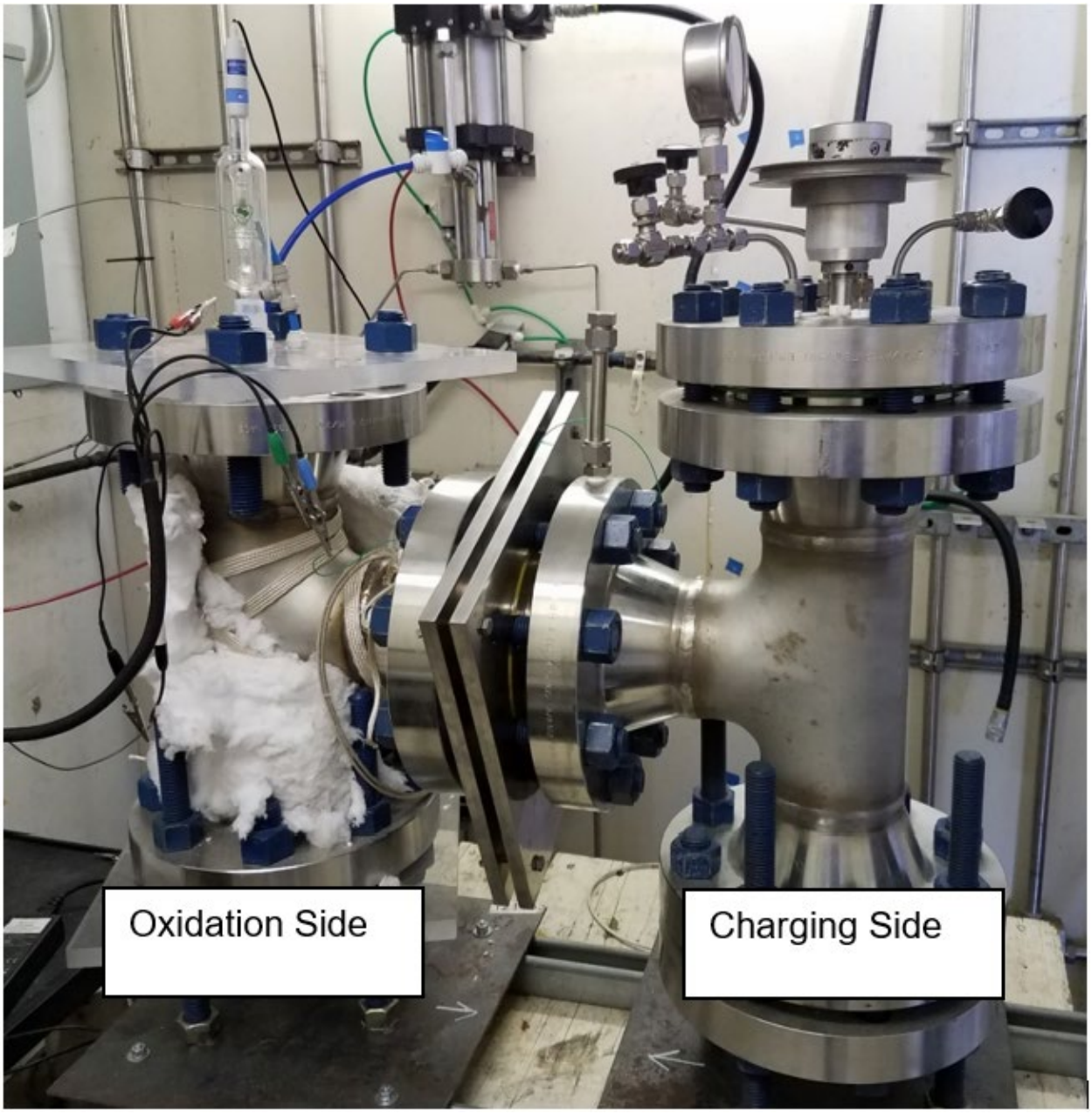

Figure B.5—High-pressure Permeation Apparatus

A 0.1 M NaOH solution was prepared separately and deaerated overnight using high-purity N_2 gas. The solution was then transferred into the oxidation side of the test apparatus using the high-purity N_2 gas to avoid O_2 inclusion. A platinum mesh was used as the counter electrode and Ag/AgCl electrode was used as the reference electrode. A +100 mV vs. SCE potential was applied on the sample and a background current was obtained in the nA range. It is beneficial to obtain a nA range background current to observe the current transient rise.

Once the background current was reached, a 100-bar (1450-psi) H_2 gas was introduced into the charging side of the permeation cell at ambient temperature. During permeation testing, H_2 diffuses through the membrane and becomes oxidized (on the oxidation side of the cell) and current is measured using a potentiostat. A current transient rise is then observed and over time reaches a steady-state (H_2

permeation current). Measurements are recorded until a steady-state current was obtained. The steady-state H_2 flux (J_{ss}) is obtained through the relationship:

$$J_{SS} = I / A \times F \tag{9}$$

where

I steady-state permeation current, Amp

A area, cm^2

F Faraday's constant, C/mol

Bibliography

[1] N.S. Muhammed, B. Haq, D. Al Shehri, A. Al-Ahmed, M. M. Rahman, and E. Zaman, "A review on underground hydrogen storage: Insight into geological sites, influencing factors and future outlook," *Energy Reports*, vol. 8, pp. 461-499, 2022/11/01, 2022.

[2] E.R. Okoroafor, S.D. Saltzer, and A.R. Kovscek, "Toward underground hydrogen storage in porous media: Reservoir engineering insights," *International Journal of Hydrogen Energy*, vol. 47, no. 79, pp. 33781-33802, 2022.

[3] B. Pan, X. Yin, Y. Ju, and S. Iglauer, "Underground hydrogen storage: Influencing parameters and future outlook," *Adv Colloid Interface Sci*, vol. 294, p. 102473, Aug 2021.

[4] A. Małachowska, N. Lukasik, J. Mioduska and J. Gebicki, “Hydrogen Storage in Geological Formations – The Potential of Salt Caverns,” *Energies*, vol. 15, issue 14, p. 5038, 2022.

[5] A. Haratian, S.E. Meybodi, M. Dehvedar, “A comprehensive review on the feasibility of largescale underground Hydrogen storage in geological structures with concentration on salt caverns,” 6th International Conference on Applied Researches in Science and Engineering, Germany 2022.

[6] API 6ACRA, *Age-hardened Nickel-based Alloys for Oil and Gas Drilling and Production Equipment*

[7] API 5CT, *Casing and Tubing*

[8] ASTM G142, *Standard Test Method for Determination of Susceptibility of Metals to Embrittlement in Hydrogen Containing Environments at High Pressure, High Temperature, or Both*

[9] ASTM E399, *Standard Test Method for Linear-Elastic Plane-Strain Fracture Toughness of Metallic Materials*

[10] ASTM E1820, *Standard Test Method for Measurement of Fracture Toughness*

[11] ASTM E1823, *Standard Terminology Relating to Fatigue and Fracture Testin*g

[12] ASTM G148, *Standard Practice for Evaluation of Hydrogen Uptake, Permeation, and Transport in Metals by an Electrochemical Technique*

[13] S.D. Pu, A. Turk, S. Lenka, S.W. Ooi, “Study of hydrogen release resulting from the transformation of austenite into martensite,” *Materials Science and Engineering: A*, vol. 754, pp. 628-635, 2019.

[14] W.M. Robertson, "Hydrogen permeation and diffusion in inconel 718 and incoloy 903," *Metallurgical Transactions A*, vol. 8, no. 11, pp. 1709-1712, Nov 1977, doi: 10.1007/bf02646873.

200 Massachusetts Avenue, NW
Suite 1100
Washington, DC 20001-5571
USA

202-682-8000

Phone Orders:	1-800-854-7179	(Toll-free in the U.S. and Canada)
	303-397-7956	(Local and International)
Fax Orders:	303-397-2740	

Information about API publications, programs and services is available on the web at www.api.org.

Product No. G21C01